# Widefield *in vivo* imaging system with two fluorescence and two reflectance channels, a single sCMOS detector, and shielded illumination

Abbreviated title: Four-color mesoscope

Patrick R. Doran[1], Natalie Fomin-Thunemann[2], Rockwell P. Tang[1], Dora Balog[1], Bernhard Zimmerman[2], Kıvılcım Kılıç[2], Emily A. Martin[2], Sreekanth Kura[2], Harrison P. Fisher[1], Grace Chabbott[3], Joel Herbert[4], Bradley C. Rauscher[1], John X. Jiang[2], Sava Sakadzic[5], David A. Boas[2], Anna Devor[2,5], Ichun Anderson Chen[2], Martin Thunemann[2]

[1]Graduate Program in Biomedical Engineering, Boston University, Boston, MA 02215, USA

[2]Department of Biomedical Engineering, Boston University, Boston, MA 02215, USA

[3]Undergraduate Program in Biomedical Engineering, Boston University, Boston, MA 02215, USA

[4]Undergraduate Program in Neuroscience, Boston University, Boston, MA 02215, USA

[5]Athinoula A. Martinos Center for Biomedical Imaging, Department of Radiology, Harvard Medical School, Massachusetts General Hospital, Charlestown, MA 02129, USA

[§]**Corresponding authors:**

Anna Devor and Martin Thunemann

610 Commonwealth Ave

Boston, MA 02215

USA

Email: adevor@bu.edu; martinth@bu.edu

## Abstract

**Significance:** Widefield microscopy of the entire dorsal part of mouse cerebral cortex enables large-scale ("mesoscopic") imaging of different aspects of neuronal activity with spectrally compatible fluorescent indicators as well as hemodynamics via oxy- and deoxyhemoglobin absorption. Versatile and cost-effective imaging systems are needed for large-scale, color-multiplexed imaging of multiple fluorescent and intrinsic contrasts.

**Aim:** Develop a system for mesoscopic imaging of two fluorescent and two reflectance channels.

**Approach:** Excitation of red and green fluorescence is achieved through epi-illumination. Hemoglobin absorption imaging is achieved using 525- and 625-nm LEDs positioned around the objective lens. An aluminum hemisphere placed between objective and cranial window provides diffuse illumination of the brain. Signals are recorded sequentially by a single sCMOS detector.

**Results:** We demonstrate performance of our imaging system by recording large-scale spontaneous and stimulus-evoked neuronal, cholinergic, and hemodynamic activity in awake head-fixed mice with a curved "crystal skull" window expressing the red calcium indicator jRGECO1a and the green acetylcholine sensor $GRAB_{ACh3.0}$. Shielding of illumination light through the aluminum hemisphere enables concurrent recording of pupil diameter changes.

**Conclusions:** Our widefield microscope design with single camera can be used to acquire multiple aspects of brain physiology and is compatible with behavioral readouts of pupil diameter.



**Key words**: mesoscope; mesoscale; cerebral cortex; fluorescence; hemoglobin absorption

42 ## Introduction

43 With the rapidly expanding list of fluorescent probes for neuronal activity and the development of
44 large-scale measurements (Abdelfattah et al. 2022), widefield microscopy has become the
45 measurement modality of choice for mesoscale studies of neuronal circuits and underlying
46 behavior when cellular resolution is not required (Bouchard et al. 2009, Mohajerani et al. 2013,
47 Ma et al. 2016b, Vanni et al. 2017, Wright et al. 2017, Couto et al. 2021). Probes available in
48 distinct spectral variants (Zhao et al. 2011) can be spectrally multiplexed for simultaneous imaging
49 of different aspects of neuronal activity (Lin and Schnitzer 2016). Using multiplexed probes for in
50 vivo widefield imaging of head-fixed mice with “crystal skull” cranial windows (Kim et al. 2016) or
51 transcranial imaging, optionally combined with thinned-skull preparations (Silasi et al. 2016),
52 provides a view of the entire dorsal part of the cerebral cortex including the primary sensory, motor
53 and higher association areas (Cramer et al. 2021, Higley and Cardin 2022).

54 In the healthy brain, increases in neuronal activity are often accompanied by increases in blood
55 flow, volume, and oxygenation in the active region. The increase in blood flow and volume occurs,
56 in large part, due to dilation of cerebral arterioles responding to vasoactive messengers released
57 by active neurons (Uhlirova et al. 2016b, Echagarruga et al. 2020). This hemodynamic response
58 increases oxygen supply beyond the actual demand leading to a net increase in blood
59 oxygenation. Both oxy- and deoxyhemoglobin (HbO and HbR, respectively) strongly absorb light
60 in the blue-green spectrum. Therefore, the hemodynamic response results in time-variant
61 modulation of fluorescence signals within that spectral range. The methods developed to correct
62 fluorescent signals for this hemodynamic artifact fall into two categories. For the first correction
63 method, enhanced green fluorescent protein (EGFP)-based indicators, including GCaMP,
64 iGluSnFR, and GRAB indicators, are excited off-peak at their isosbestic point in the 390-420 nm
65 range. When excited at these wavelengths, fluorescence emission is independent from the
66 analyte concentration (i.e., [$Ca^{2+}$], [Glutamate], etc.), but affected by hemodynamic changes

67 (Dana et al. 2019, Jing et al. 2020). This signal can then be regressed out of the analyte-
68 dependent signal to remove hemodynamic artifacts. Correction methods measuring changes in
69 hemoglobin absorption use either a single reflectance measurement at 520-530 nm or estimate
70 changes in HbO and HbR concentrations (ΔHbO] and ΔHbR]) from simultaneous acquisition of
71 light absorption from at least two wavelengths (Ma et al. 2016a). Furthermore, quantitative
72 estimates of Δ[HbO] and Δ[HbR] are important measurables on their own; they aid in
73 understanding cerebrovascular physiology and interpretation of non-invasive imaging signals
74 generated through, for example, functional magnetic resonance imaging (fMRI) (Uhlirova et al.
75 2016a).

76 Current stationary widefield imaging setups typically use light-emitting diodes (LEDs) with
77 sequential illumination, one or two low-noise, high-sensitivity scientific CMOS cameras, and low
78 (smaller than 2x) magnification optics with a large field of view (Cardin et al. 2020). Experimental
79 demands led to various adaptions of this basic blueprint. In systems dedicated for widefield
80 calcium imaging with EGFP-based indicators, blue LEDs (450-480 nm) are used for fluorescence
81 excitation, with light delivered through the objective lens or through side-illumination in some
82 cases. Hemodynamic correction of green fluorescence signals either uses off-peak (390-420 nm)
83 fluorescence excitation (Mohajerani et al. 2013, Lerner et al. 2015, Allen et al. 2017, Musall et al.
84 2019, Jacobs et al. 2020, Lake et al. 2020, MacDowell and Buschman 2020, Couto et al. 2021,
85 Peters et al. 2021, Zatka-Haas et al. 2021) or is based on reflectance measurements at
86 520-530 nm (Wekselblatt et al. 2016, Vanni et al. 2017, Wright et al. 2017, Gilad et al. 2018, Mitra
87 et al. 2018). Several groups incorporated a second fluorescence channel with excitation at 560-
88 590 nm to enable two-color fluorescence imaging of red fluorescent calcium indicators like
89 jRCaMP1b or jRGECO1a in combination with either EGFP-derived indicators such as GCaMP6
90 (Gribizis et al. 2019), $GRAB_{ACh}$ (Lohani et al. 2022), or flavoprotein autofluorescence (Wang et al.
91 2022, Raut et al. 2023). Widefield imaging systems dedicated to the investigation of

neurovascular interactions typically combine imaging of green (Ma et al. 2016b, Matsui et al. 2016, Wright et al. 2017, Mitra et al. 2018, Valley et al. 2020, Sunil et al. 2023), red fluorescent indicators (Park et al. 2020, Raut et al. 2023, Shahsavarani et al. 2023), or green and red fluorescent indicators (Wang et al. 2022) with reflectance imaging for ΔHbO] and ΔHbR] estimation at two or three wavelengths, typically in the range of 525-565 nm and 590-625 nm. Light for reflectance imaging is delivered directly from one or more multi-color light engines (Wright et al. 2017, Mitra et al. 2018, Shahsavarani et al. 2023), through a single light guide (Park et al. 2020), through an illumination ring (Harrison et al. 2009, White et al. 2011, Jacobs et al. 2020), or through several optical fibers connected to a single light source (Valley et al. 2020) to illuminate the sample surface at an angle. Some researchers report the use of linear polarizers in front of the light sources to minimize specular reflection from the glass window (White et al. 2011, Wright et al. 2017, Mitra et al. 2018). Experiments involving behavioral tasks or visual stimulation, different solutions to block illumination light from reaching the animal's eyes have been reported, for example through implanted light shielding (Makino et al. 2017, Valley et al. 2020), custom light-shielding between objective and headplate (Couto et al. 2021, Nietz et al. 2023), or imaging stage design (Padawer-Curry et al. 2023).

Here, we describe a versatile widefield imaging system that enables two-color fluorescence imaging in addition to concurrent acquisition of two reflectance channels for quantitative estimation of ΔHbO] and ΔHbR] with a single sCMOS detector. Specular reflections from curved glass cranial windows that interfere with reflectance imaging are minimized using diffuse illumination with 525- and 625-nm light for reflectance imaging by combining a custom-built ring illuminator with an aluminum hemisphere between objective and cranial window. In addition, the aluminum hemisphere shields illumination light to prevent it from reaching the animal's eyes and thereby avoiding unwanted visual stimulation of the animal. We provide optical design blueprints, a wiring diagram, a timing chart, data acquisition software, and an inventory of all parts. We

117 demonstrate the performance of our new widefield microscope in awake mice expressing the
118 mApple-based calcium indicator jRGECO1a (Dana et al. 2016) and the EGFP-based
119 acetylcholine (ACh) probe $GRAB_{ACh3.0}$ (Jing et al. 2020).

120 ## Results

121 We designed and manufactured a widefield imaging system with a field of view of 10×10 $mm^2$
122 covering the dorsal cortex of a mouse. We use a single sCMOS detector for sequential recording
123 of two fluorescent indicators (here: EGFP-derived $GRAB_{ACh3.0}$ and mApple-derived jRGECO1a)
124 as well as hemoglobin absorption at 525 and 625 nm at an effective frame rate of 10 Hz or better
125 without changes in the configuration of the emission path. **Figure 1** and **Supplementary Figure**
126 **1** provide an overview of the system layout and illustrate the spectral properties of the light
127 sources and filter elements together with HbO and HbR absorption spectra as well as jRGECO1a
128 and $GRAB_{ACh3.0}$ excitation and emission spectra. For fluorescence excitation, we use epi-
129 illumination through the objective lens. A 470-nm LED with a maximal power of 3.7 W provides
130 light for $GRAB_{ACh3.0}$ excitation, which is filtered through a 466/40 nm excitation bandpass filter,
131 resulting in a maximal power of 403 mW at the sample surface. For jRGECO1a excitation, we use
132 light from a 565-nm LED with a maximal power of 8.6 W which is filtered through a 560/14 nm
133 excitation bandpass filter reaching a maximal power of 75 mW at the sample surface. A secondary
134 peak in the 565-nm LED spectrum at ~425 nm is removed by an additional 450-nm longpass filter
135 in the excitation path (**Figure 1A**). The collimated and filtered light is coupled into the infinity space
136 using a multiband dichroic mirror (488/561 nm, 'main dichroic'). This, in combination with a multi-
137 band 'detection filter' (523/610 nm), allows $GRAB_{ACh3.0}$ and jRGECO1a fluorescence at 500-
138 540 nm and 580-640 nm, respectively, to reach the sCMOS detector while blocking excitation
139 light at 440-480 nm and 550-570 nm from reaching the camera (**Figure 1D, E, G**). Typical powers
140 at the sample surface during image acquisition were 90-177 mW and 68-75 mW for 470 nm and
141 565 nm at illumination times of 3-6 ms, respectively. We observed no or minimal bleaching over
142 continuous acquisition periods of up to 30 minutes. The wavelengths for hemoglobin absorption
143 imaging are within the respective emission bands of the green (525 nm) and red (625 nm)
144 fluorophore (**Figure 1F**). The LEDs used for hemoglobin absorption imaging are placed in a

145 custom-designed reflectance illumination ring (RIR) located between the objective lens and the
146 sample surface (**Figure 1B** and **Supplementary Figure 1D**). The RIR contains six 525-nm LEDs
147 and six 625-nm LEDs positioned at equal distances with maximal powers of 170 mW and 371 mW
148 per LED, respectively. To enable a simple procedure for estimation of Δ[HbR] and Δ[HbO], we
149 placed 10-nm bandpass filters in front of each LED. This leads to a maximal power of 39.5 mW
150 (525 nm) and 51 mW (625 nm) at the sample surface. During image acquisition, typical powers
151 at the sample surface were 10.5 mW and 4.4 mW for the 525-nm and 625-nm LEDs at 3-ms
152 illumination times.. We placed a hollow aluminum hemisphere between the RIR and the sample
153 surface internally reflecting the light of the 525-nm and 625-nm LEDs. For imaging, the opening
154 of the hemisphere is brought close to the sample surface achieving diffuse illumination and
155 efficiently eliminating most reflections from the curved glass window covering the brain surface.

156 With the chosen sCMOS camera working in rolling shutter mode, we ensure that the LEDs emit
157 light only when all rows of the sCMOS chip are simultaneously exposed. Therefore, we control
158 the LED drivers with two digital trigger signals combined through a logical AND gate integrated
159 circuit (IC) (**Figure 1C**). The first input to the AND gate IC is generated by the camera and is in
160 'high'-state when all rows are being exposed; the second input is generated by the microscope
161 control computer and selects the respective LED wavelength to be switched on (**Figure 1C**). Only
162 when both signals are in 'high' state, the LED power supply receives a trigger signal to switch the
163 respective LED on. Timing delays of the AND gate IC and the LED driver are <9 ns and <100 μs,
164 respectively, enabling virtually delay-free LED power switches for typical exposure times of 2-
165 8 ms per individual LED.

166 The imaging setup is controlled through a DAQ interface programmed via MATLAB. The main
167 acquisition script generates digital trigger signals controlling the imaging setup based on exposure
168 time, which can be different for every wavelength, acquisition rate, and total acquisition time.
169 Additional triggers are generated to synchronize or control external devices such as stimulus

170 apparatuses, behavioral cameras, electrophysiology recording equipment, and behavioral control
171 devices. The currents of the individual LEDs are set in MATLAB and sent via a USB-based
172 remote-control interface to the LED drivers. The sCMOS camera is controlled through the
173 manufacturer's software where parameters such as field of view and on-camera pixel binning are
174 set. This software also drives image acquisition; however, the camera is set to respond to
175 exposure triggers generated by the DAQ interface, with the (variable) trigger length determining
176 the exposure time. During acquisition, the DAQ interface records feedback signals from camera,
177 microscope control, and external devices allowing synchronization of data streams during off-line
178 post-processing and analysis.

179 While our single-camera approach reduces complexity and cost, we use multiband filters to image
180 two fluorophores present in the sample at the same time. The lack of spectral separation on the
181 emission side can potentially create crosstalk when fluorophores are excited off-resonance. Note
182 that both fluorophores undergo dynamic changes in fluorescence intensity, so the degree of
183 crosstalk will vary in time and space. Published spectra show that $GRAB_{ACh3.0}$ (or EGFP) is
184 essentially not excited at 565 nm, while jRGECO1a (or mApple) fluorescence is excited at
185 470 nm. To quantify the amount of crosstalk under well-controlled conditions, we collected images
186 of purified EGFP and mApple proteins with various combinations of illumination power and
187 exposure time for both the 470-nm and 565-nm LEDs. In line with the published spectra, we
188 observed that the 565-nm LED practically does not excite purified EGFP while mApple shows
189 fluorescence when excited with the 470 nm LED (**Supplementary Figure 2A** and **B**). Based on
190 this *in vitro* calibration with EGFP and mApple and the typical acquisition parameters we used for
191 *in vivo* imaging in $GRAB_{ACh3.0}$- and jRGECO1a-expressing animals, we determined that the level
192 of crosstalk of $GRAB_{ACh3.0}$ to fluorescence measured upon 565-nm excitation is <1%, while
193 fluorescence from jRGECO1a contributes about 3-9% to the fluorescence intensity measured
194 upon 470-nm excitation (**Supplementary Figure 2**; see **Appendix B** for a detailed discussion of

195 the crosstalk analysis). To verify that the degree of crosstalk is similar in recordings from awake
196 mice expressing $GRAB_{ACh3.0}$ and jRGECO1a, we applied a simplified correction approach that
197 does not incorporate dynamic changes of hemoglobin absorption on fluorescence excitation and
198 emission (details in **Appendix B**). After applying the correction, we used cross-correlation
199 analysis to verify that the degree of crosstalk is within the same range as established under in-
200 vitro conditions (**Supplementary Figure 3**). Here, it should be noted that high correlation between
201 $GRAB_{ACh3.0}$ and jRGECO1a signals is expected primarily due to their underlying physiological
202 covariance (Lohani et al. 2022) and is only influenced to a small degree by optical crosstalk, as
203 shown in the analysis. However, while the in-vitro calibration provides us with the parameters
204 necessary to perform crosstalk correction of in-vivo data, we decided not to further use crosstalk
205 correction for the recorded in vivo data as it likely will add additional noise without sufficient benefit
206 – at least under the experimental conditions present in this study (see **Appendix B** for further
207 discussion).

208 In addition, it has been reported for mApple-based calcium indicators like jRGECO1a that
209 illumination with blue light leads to photo-switching, which causes a reversible, calcium-
210 independent increase in fluorescence intensity (Dana et al. 2016). In a control experiment with an
211 awake jRGECO1a-expressing mouse, we did not observe jRGECO1a photo-switching under
212 470-nm illumination conditions typical for two-color fluorescence imaging in $GRAB_{ACh3.0}$- and
213 jRGECO1a-expressing mice. However, when the 470-nm illumination intensity was increased by
214 an order of magnitude compared to typical imaging conditions, we observed photo-switching of
215 jRGECO1a (**Supplementary Figure 4**).

216 To demonstrate the capabilities of our new imaging system design under in-vivo conditions, we
217 recorded spontaneous and stimulus-induced changes in neuronal calcium, ACh, and
218 hemodynamic signals in awake head-fixed mice expressing jRGECO1a and $GRAB_{ACh3.0}$ (**Figure**
219 **2**). Mice were implanted with a curved glass cranial window exposing both hemispheres of the

220 dorsal cortex while leaving the bone in-between the two hemispheres above the superior sagittal
221 sinus intact (Kilic et al. 2020) (**Figure 2A**). Images were registered to the Allen Mouse Common
222 Coordinate Framework (Wang et al. 2020) to generate time courses from pre-defined regions of
223 the dorsal cortex. Measurements of spontaneous activity show a high correlation between
224 neuronal calcium and ACh time courses (**Figure 2B** shows right secondary motor cortex), which
225 is consistent with published results (Lohani et al. 2022). We then recorded the response to a
226 sensory stimulus consisting of a 2-s, 3-Hz air puff sequence (20 repetitions, 25 s inter-stimulus
227 interval) delivered to the right whisker pad (**Figure 2C-E**). Ratio maps show neuronal activation
228 and functional hyperemia in the contralateral barrel cortex (green ROI in calcium map, **Figure**
229 **2C**). The stimulus-averaged time course calculated from the contralateral barrel cortex shows that
230 the imaging system operates at sufficient signal to noise ratio to record the neuronal calcium
231 response to the six individual air puffs comprising one stimulus train (**Figure 2D**). Despite high
232 trial-to-trial variability (**Figure 2E**), which is consistent with published widefield imaging studies in
233 awake mice (Musall et al. 2019), responses to individual air puffs are still discernible in individual
234 trial recordings. The time course of the hemodynamic response shows a broad peak and post-
235 stimulus undershoot. The hemodynamic correction we apply to the green fluorophore
236 compensates for darkening that occurs when hemoglobin levels increase. **Supplementary**
237 **Figure 5** compares the trial averaged ACh time courses with and without correction for
238 hemodynamic artifacts.

239 With a unit price of >$20,000, the sCMOS camera is the most expensive component of the
240 imaging system. To show how the system performance is affected by camera choice, we repeated
241 the experiment shown in **Figure 2** with a CMOS camera costing aound $750 (**Supplementary**
242 **Figure 6**). Time courses of signals averaged from spatially connected pixels in a region of interest
243 show stimulus-evoked and spontaneous changes in neuronal calcium, ACh, and hemodynamic
244 signals (**Supplementary Figure 6B, D, E**). On the other hand, we observed spatially structured

245 noise across the field of view (compare **Figure 2C** with **Supplementary Figure 6C**) that could
246 impact pixel-based analysis methods.

247 The aluminum hemisphere in-between the cranial window and the imaging system reflects 525-
248 and 625-nm light and provides diffuse illumination minimizing specular reflections at the curved
249 glass window that interfere with reflectance imaging. Inhomogeneities of signal intensity across
250 the sample surface are likely occur due to the curvature of the 'crystal skull' glass window (**Figure**
251 **2A**). While enabling diffuse illumination, the aluminum hemisphere also acts as a shield
252 preventing the strobing illumination light from reaching the mouse's eyes. For example, four-color
253 imaging with an effective acquisition rate of 10 Hz would produce an undesired visual stimulus at
254 40 Hz. To illustrate the shielding effect, we recorded changes of the animal's pupil diameter during
255 mesoscopic imaging in presence or absence of the aluminum hemisphere (**Figure 3**). For this
256 experiment, a behavioral camera recorded the pupil diameter continuously while widefield
257 illumination across the four wavelengths at 40 Hz was switched on and off at 60-s intervals; we
258 recorded 20 off-to-on and on-to-off transitions per test. The images shown in **Figure 3A** show the
259 pupil before and after turning the illumination on; **Supplementary Video 1** shows a recording of
260 the off-to-on transition with and without hemisphere. **Figure 3B** shows representative 2-min time
261 series covering the off-to-on and on-to-off transitions in presence or absence of the hemisphere.
262 Without the hemisphere, pupil size measurements are largely dominated by the state of widefield
263 illumination. In the presence of the hemisphere, pupil size changes are largely independent from
264 widefield illumination (**Figure 3C**). Then, we compared the relative change in pupil size from 1.5-
265 0.5 s before versus 2-3 s after start of widefield illumination averaged over 20 transitions and
266 observe a significantly larger drop in pupil size without the hemisphere ($p<0.001$; t-test; **Figure**
267 **3D**). Pupil tracking is often used as an important variable to define behavioral states (Vinck et al.
268 2015, Reimer et al. 2016) and it is therefore desirable to combine pupil recordings and mesoscale
269 imaging (Shahsavarani et al. 2023). In our system, the hemisphere eliminates interference of

widefield illumination on behavioral recordings and enables high-quality measurements of pupil dynamics during mesoscale imaging.

## Discussion

Here, we describe a new widefield microscope design for mesoscopic imaging of dorsal mouse cortex. Several groups describe widefield calcium imaging with a single fluorescent indicator and concurrent hemodynamic imaging, while other groups describe two-color fluorescence widefield imaging without hemodynamic imaging, while we identified one report describing a system for combined two-color fluorescence and hemodynamic imaging using two cameras (Wang et al. 2022). Compared to previous publications, our system has several unique features:

First, the system enables quasi-simultaneous imaging of two spectrally distinct fluorophores (here: EGFP-based $GRAB_{ACh3.0}$ and mApple-based jRGECO1a) together with quantitative estimates of Δ[HbO] and Δ[HbR] via two-color absorption imaging on a single detector. Changes in [HbO] and [HbR] are used to correct hemodynamic artifacts of the recorded fluorescence signals. Further, we can use them to study the relationship between cortical hemodynamics and different aspects of brain activity, such as neuronal firing and neuromodulation thereby gaining further insights into brain state-dependent regulation of cerebral blood flow and metabolism (Machler et al. 2021).

Second, we use a single detector. Using one camera drastically reduces the overall cost to build the system but requires sequential image acquisition for every wavelength (here: four wavelengths). We achieve sufficient SNR with negligible spectral crosstalk at a 10 Hz acquisition rate, which is within the range for widefield imaging studies in awake animals (Lake et al. 2020, Lohani et al. 2022).

Finally, the illumination light is contained within an aluminum hemisphere. Besides providing diffuse illumination for light from 525- and 625-nm LEDs to minimize reflections at the glass window, the hemisphere blocks most of the illumination light from the animal's view. This prevents interference with behavioral measurements of pupil diameter as well as unwanted stimulation of

296 the visual system. Pupil size measurements are often used as a non-invasive, indirect readout of
297 alertness (Joshi et al. 2016, Reimer et al. 2016). We expect our shielded illumination design will
298 enable seamless integration of mesoscale imaging with behavioral experiments based on visual
299 stimulation (Vinck, Batista-Brito et al. 2015, Peters, Fabre et al. 2021) and virtual reality (Pinto,
300 Rajan et al. 2019).

301 The overall cost to build our widefield imaging system with the components used is around
302 $45,000, with the camera comprising the bulk of the cost (~$25,000). While this is a lower price
303 than for typical commercially available widefield imaging systems, modifications could further
304 reduce the overall cost of the system. Depending on the brightness of the used fluorophores, their
305 expression level, as well as experimental demands, sufficient imaging performance could be
306 achieved with a less expensive camera (see **Supplementary Figure 6**). Furthermore, we used
307 commercially available LED drivers as well as commercially available LEDs for fluorescence
308 excitation. Using a custom design or already available open-source components with similar
309 performance characteristics, especially regarding their response time to digital triggers, could
310 further reduce the overall cost (see, e.g., (Harrison et al. 2009)).

311 Our imaging system can easily be modified or expanded to suit the requirements of different
312 experimental studies; changing a LED and the corresponding optical filters will allow combining
313 other fluorescent indicators if they are spectrally separated. This would, for example, allow
314 integration of calcium indicators excited with near-infrared light (Qian et al. 2020). As the spectral
315 diversity of genetically encoded molecular probes expands, widefield imaging with three spectrally
316 separated fluorescent indicators might soon become a feasible approach. Furthermore, we and
317 others combined mesoscale imaging with extracellular electrophysiology, providing simultaneous
318 access to cortical network activity as well as single- or multi-unit activity in targeted cortical and
319 subcortical areas (Allen et al. 2017, Thunemann et al. 2018, Lu et al. 2023).

320 Our current system design has the following limitations. First, despite aiming to minimize specular
321 reflections and illumination inhomogeneity of 530- and 630-nm LEDs through diffuse illumination,
322 we still observe inhomogeneous levels of absolute image brightness across the field of view. In
323 practice, however, some variation of absolute brightness will not affect the readout of relative (i.e.,
324 intensity-normalized) changes in fluorescence or absorption, except for potentially reduced
325 signal-to-noise levels in darker regions of the image. A possible way to further improve illumination
326 homogeneity of both reflectance and fluorescence illumination is the incorporation of an
327 integration device with uniformity correction, such as EUCLID (Celebi et al. 2023) into our imaging
328 system. Further, uneven signal intensity in the medial-to-lateral direction is due to the curvature
329 of the glass window covering the cranial exposure (see **Figure 2A**). Use of curved glass also
330 causes different cortical depths to match the focal plane of the imaging system, which potentially
331 introduces spatially heterogenous sampling bias. Here, use of adaptive lens optics, such as meta-
332 lenses (Yang et al. 2023) could improve uniformity of illumination and could be used to match the
333 focal plane across the field of view. Designing an imaging system with a single camera reduces
334 overall system cost. However, the use of two cameras would allow for higher acquisition rates
335 through spectral multiplexing. Further, the dual-band dichroic mirror and emission filter cut the
336 available spectral bandwidth of the EGFP/GRAB$_{ACh3.0}$ emission band (500-540 nm) and the
337 mApple/jRGECO1a excitation band (550-570 nm). This potentially enables crosstalk due to off-
338 peak excitation of the red fluorophore (see further discussion in **Appendix B**). However, with the
339 fluorophores at the expression levels used, we achieve sufficient SNR with negligible spectral
340 crosstalk at a 10-Hz acquisition rate, which is within the range of appropriate temporal resolution
341 for widefield imaging studies in awake animals (Lake et al. 2020, Lohani et al. 2022). Furthermore,
342 the extension of the imaging system by a second camera requires minimal modifications to the
343 overall layout, allowing for higher acquisition speeds, if desired. Another consideration during the
344 design of our system was the use of lasers instead of LEDs for excitation of the green and red
345 fluorescent proteins. While less expensive, LEDs have a broad emission spectrum that requires

346 clean-up through excitation filters. This limits the emitted light to the usable spectral range (see,
347 e.g., **Figure 1E**, 565-nm LED) leading to an overall reduction in the available power compared to
348 the nominal output (75 mW versus 8.6 W for the 565-nm LED), potentially requiring longer
349 integration times to achieve sufficient SNRs. Here, use of a laser would enable excitation at higher
350 power levels, if required. A drawback of using lasers instead of LEDs would be a substantial
351 increase in the cost of the system.

352 In summary, given the versatility of our system and the comparatively low cost in contrast to
353 commercial intravital imaging setups, we expect our widefield imaging system design to become
354 a useful platform for neurovascular studies in the neuroscience and neurophotonics community.

# Methods

## Experimental animals

All procedures were conducted with approval from Boston University Institutional Animal Care and Use Committee and in accordance with the National Institutes of Health Guide for the Care and Use of Laboratory Animals. Standard rodent chow and water were provided ad libitum. Mice were housed in a 12-hour light cycle with lights turning on at 7:30 AM. We used three female mice of the Thy1-jRGECO1a GP8.20 (Dana et al. 2016, Dana et al. 2019) line; cortex-wide $GRAB_{ACh3.0}$ expression was induced by injection of 1.5 µL AAV9-hSyn-$GRAB_{ACh3.0}$ (WZ Biosciences, $3.06\times10^{13}$ GC/mL) into each transverse sinus (3 µL per animal) of 1-day old neonates according to procedures described in Lohani et al. (2022).

Headpost implantation and craniotomy in adult (8-16 week old) animals follows procedures described in Kilic et al. (2020). Briefly, a custom-designed headpost machined from titanium was attached to the cranium and a modified crystal skull curved glass window was used to replace the dorsal cranium on both hemispheres (Kim et al. 2016). Prior to surgery, the original curved glass (12 mm width, labmaker.org) was cut in half to obtain separate glass pieces for each hemisphere. Following the implantation procedure, a silicone plug was placed on top of the glass window and a 3D-printed cap was fixed to the headpost to prevent heat loss. Mice were allowed to recover for at least one week following surgery before behavioral training commenced.

To adapt mice to be comfortable under head fixation, animals were handled until they remained calm in the gloved hand of the investigator. Mice were then head-fixed for increasing periods while they received a reward of sweetened condensed milk. Data acquisition was started when animals tolerated one hour of head fixation.

## Imaging system optical components

The imaging system is assembled from standard optomechanical components compatible with

379 two-inch lens tubes. The imaging system is placed on an elevated platform (61×61 cm, Thorlabs,
380 MB2424) on a vibration-isolating table.
381 A 470-nm LED (Thorlabs, SOLIS-470C) is used to excite $GRAB_{ACh3.0}$ and a 565-nm LED
382 (Thorlabs, SOLIS-565C) is used to excite jRGECO1a. A 466/40 nm excitation filter (Semrock,
383 FF01-466/40, diameter 50 mm) is placed in front of the 470-nm LED and a 560/14 nm excitation
384 filter (Semrock, FF01-560/14, diameter 50 mm) is placed in front of the 565-nm LED. A dichroic
385 mirror combines excitation light from 565-nm and 470-nm LEDs (Semrock, FF520-Di02,
386 50 x 72 mm). The output of these LEDs is filtered through a 450-nm longpass filter (Chroma,
387 AT450lp) to remove low wavelength light from the 565-nm LED that leaks through the primary
388 excitation filter. A 45-degree mirror (Thorlabs, PF20-03-P01, diameter 50.8 mm) reflects
389 excitation light down towards the mouse and reflects emitted light into the plane of the camera. A
390 dual-band 'main dichroic' beam splitter (Semrock, Di03-R488/461, 50 x 72 mm) reflects excitation
391 light towards the mirror and transmits emitted light towards the camera. A dual-band emission
392 filter (Semrock, FF01-523/610, diameter 50 mm) is placed between a dichroic mirror and camera.
393 A tube lens (Olympus, MVX-TLU-MVX10) projects the image onto the sCMOS camera (Andor,
394 Zyla 4.2P-CL10 or Sona 4.2B-6).

395 An objective lens (Olympus, ZDM-1-MVX063) focuses the fluorescence excitation light onto the
396 brain for epi-illumination and projects the emitted light towards the camera. The objective lens is
397 surrounded by the reflective illumination ring (RIR) assembly, which contains six equally spaced
398 525-nm LEDs (CREE LED, XBDGRN-00-0000-000000C02) and six equally spaced 625-nm LEDs
399 (CREE LED, XBDRED-00-0000-000000701) for reflectance imaging. Bandpass filters were cut
400 to 9.4-mm diameter and placed in front of the reflectance LEDs. These filters are 532/10 nm
401 bandpass filters (Edmund Optics, 65094) for the 525-nm LEDs and 632/10 nm bandpass filters
402 (Edmund Optics, 65105) for the 625-nm LEDs. Six Peltier elements (Ferro Tec, 81044) controlled
403 by a feedback-controlled temperature controller (Thorlabs, TED200C) actively cool the LEDs in

404 the RIR to maintain the LEDs at room temperature during data acquisition. Temperature is
405 measured on the LED ring with a 10-kΩ thermistor (TDK, NTCG163JF103FT1). Heat from the
406 Peltier elements is transferred to a custom heat sink made of aluminum. The RIR allows fixation
407 of custom hemisphere made of aluminum (bead-blasted) with a 15-mm opening located directly
408 above the cranial window.

409 To perform imaging tests with a different camera model (ac1920-150uc, Basler with Python 2000
410 CMOS chip from ON semiconductor in global shutter mode), a 45-degree mirror (Edmund Optics,
411 83-538) behind the detection filter was used to divert the light path to a second camera arm with
412 alternative tube lens (ThorLabs, TTL180-A). The camera was controlled through the
413 manufacturer's software (Pylon Viewer); 4x4 binning (sum) with analog gain disabled were used
414 with exposure times set to 6 ms for all frames.

415 **Control of imaging acquisition**

416 We use a computer-controlled DAQ device (National Instruments, PCIe-6363) to operate the
417 imaging system. The DAQ device is connected to two I/O connector boards (National Instruments,
418 CB-68LPR) inside a control interface box. The control interface relays a DAQ-generated exposure
419 trigger to the camera. An integrated circuit with an OR gate (Texas Instruments, SN74AHC32N)
420 within the control interface receives the "Fire ALL" trigger from the camera as an input. The "Fire
421 ALL" trigger is positive when the exposure state overlaps for all rows in the rolling shutter mode.
422 The output of the OR gate is the common input to an integrated circuit with four AND gates (Texas
423 Instruments, SN74AC08N). The second – wavelength-specific – input to each individual AND
424 gate is the LED selection trigger generated by the DAQ system. Each output of the AND gate
425 connects to one LED driver (Thorlabs, DC2200) controlling one type of LED. During normal
426 operation of the imaging system, the "Fire ALL" trigger controls when the LED turns on. The other
427 input to the OR gate is a camera bypass trigger that allows the LEDs to be triggered while the

428 camera is off. We use a custom MATLAB script to control the DAQ system. We used image
429 capture software (Andor, SOLIS) to control camera and image acquisition.

430 The animal was positioned under 525-nm illumination and the platform carrying the animal was
431 adjusted to bring the brain surface into focus. Then, the aluminum dome is lowered to minimize
432 the distance between its opening and the brain surface. Illumination intensities (i.e., LED currents)
433 were adjusted to bring image intensities into the dynamic range of the camera at 16-bit image
434 depth. The acquisition window was cropped to the size of the field of view; image height (number
435 of rows) was a variable entered into the MATLAB script controlling image acquisition: the length
436 of the period when all rows are exposed ("FIRE all") depends on image height and requires
437 adjustment of the camera exposure trigger generated by the DAQ system. Typical image sizes
438 were 460×360 pixels with a 9.2×7.2 mm field of view and 20-μm resolution at 4×4 binning. Based
439 on selected exposure times and frame rate, the MATLAB script calculates the total number of
440 frames per acquisition run; this number is entered into the image capture software. The camera
441 is set to "External Exposure" mode and image acquisition is started. Then, execution of the
442 MATLAB script is started causing the DAQ interface to send LED selection and camera triggers
443 to the control interface.

444 **Sensory stimulation and behavioral recordings**

445 The MATLAB acquisition script generates additional triggers for synchronization with behavioral
446 apparatuses, such as to deliver stimuli by puffing compressed air to the animals' whiskers. Stimuli
447 are defined by duration, frequency, repetitions, interstimulus interval for individual stimuli and
448 sequences of pre-stimulus baseline, stimulus, and post-stimulus observation period. Based on
449 these parameters, the MATLAB script calculates the required imaging time and number of
450 images. For air puff stimuli, the 5-V trigger is sent to a picopump (WPI, PV830) connected to a
451 2-mm diameter plastic tube that terminates in a glass capillary to deliver pressurized air to the
452 mouse whiskers.

453 The animal's face and whiskers are recorded during imaging with a CMOS camera (Basler,
454 acA1920-150uc) through a variable zoom lens (Edmund Optics, 67715). A 940-nm LED
455 (Thorlabs, M940L3) continuously illuminates the animal, and a 920-nm long pass filter prevents
456 light from the microscope from contaminating the camera recording. The mesoscope control
457 system triggers the CCD camera to acquire a single frame during each acquisition cycle.

458 An accelerometer (Analog Devices, ADXL335) is placed underneath the mouse bed to record
459 animal's motion. The accelerometer generates analog signals for motion in X, Y and Z direction
460 which are recorded by a separate DAQ system (NI, USB-6363) receiving a synchronization signal
461 from the mesoscope control system.

462 **Image processing**

463 The camera control software (Solis, Andor) stores the acquired images as raw data ('.dat')
464 together with metadata files ('.ini' and '.sifx'). For all subsequent import and processing steps, we
465 use MATLAB. Raw image data is loaded into MATLAB, bypassing conversion into image (.tif) files
466 by the camera software and enabling multi-stream data import from high-performance solid-state
467 drives with MATLAB's multi-processor environment. For all channels, a baseline image
468 representing the temporal average of all images for that channel is generated. For fluorescence
469 channels, ΔF/F images are computed on a pixel-by-pixel basis by dividing each image by the
470 baseline image. After calculating ΔF/F, linear trends are removed from the time course of each
471 pixel using the MATLAB function "detrend". The modified Beer-Lambert law is used to calculate
472 changes in HbO and HbR concentrations from 525 nm and 625 nm reflectance (see
473 implementation for MATLAB's multi-processor environment in **Appendix A**). Estimated Δ[HbO]
474 and Δ [HbR] are used to correct green fluorescence measurements for artificial intensity changes
475 caused by dynamic changes in excitation and emission light absorption by hemoglobin. The
476 correction method has been described in Ma et al. (2016a) and its implementation is further
477 detailed in **Appendix A**. In this correction approach, the measured fluorescence is equal to the

478 artifact-free change in fluorescence multiplied by a correction factor containing the pathlength in
479 tissue and the tissue absorption coefficient. Pathlengths have been previously estimated based
480 on Monte-Carlo simulations (Ma et al 2016). Since hemoglobin accounts for most of the light
481 absorption in brain tissue, light absorption depends largely on Δ[HbO] and Δ[HbR] and the known
482 HbO and HbR extinction coefficients at the respective wavelengths of fluorescence excitation and
483 emission. We calculate the light absorption coefficient for every pixel at every time point based
484 on our estimations of Δ[HbO] and Δ[HbR] and apply it to correct for hemodynamic darkening of
485 ΔF/F in the green (EGFP/$GRAB_{ACh3.0}$) channel.

486 Measurements with several consecutive trials are interpolated at 100-ms intervals using a time
487 vector relative to the stimulus onset. Trial-averaged ratio maps are calculated by averaging
488 individual time courses across trials.

489 Behavioral video recordings are stored as image sequences and imported into MATLAB. To
490 calculate pupil size, an elliptical region is drawn defining the eye and an intensity threshold is
491 manually defined. The pupil size is calculated as the number of pixels below the threshold. The
492 resulting time series is normalized to its maximal and minimal pupil size within the recording.

493 ***In vitro* crosstalk calibration**

494 Solutions of purified 0.03 mg/mL EGFP (Abcam, ab84191) and 0.4 mg/mL mApple (kindly
495 provided by Ahmed Abdelfattah) in phosphate-buffered saline (PBS) were prepared prior to
496 imaging. 30-μL samples of EGFP, mApple, or PBS-only control solution were each injected into
497 one channel of separate 6-channel slides (ibidi, μ-Slide VI – Flat). The center of the fluorophore-
498 filled channel was focused under the widefield imaging system before starting image acquisition
499 for each slide. Illumination during an imaging sequence alternated between the 470-nm and
500 565-nm LEDs while stepping through a series of camera exposure times and increasing LED
501 currents. Three trials were conducted for each sample, with the position of the slide under the

502 objective being shifted between trials to account for intensity variations. To calculate the
503 fluorescence intensity, pixel values were averaged over a region of interest covering the center
504 of the fluorophore-containing channel. Then, we took the mean of the three trials per condition
505 and subtracted the fluorescence intensity of the PBS control. Further analysis of crosstalk is
506 detailed in **Appendix B**.

507 **Photo-switching of jRGECO1a**

508 A variant of the MATLAB acquisition script was used to create two types of acquisition cycles:
509 One cycle includes 470-nm illumination and disables image acquisition (no camera exposure
510 trigger and bypassing the 'FIRE ALL' trigger), while the other cycle does not include 470-nm
511 illumination but normal image acquisition. The combination of both cycles enables intermittent
512 470-nm illumination cycles at variable frequencies. Image analysis is performed on baseline-
513 normalized time courses averaged from all pixels across the brain surface.

514

## Conflict of Interest

The authors declare that they have no conflicts of interest.

## Acknowledgements

We thank Ahmed Abdelfattah for generously providing purified mApple fluorescent protein for calibration of our imaging system. We gratefully acknowledge support from the NIH (BRAIN Initiative R01MH111359, BRAIN Initiative U19NS123717, R01DA050159, R01NS108472). Patrick Doran was supported by the Ruth L. Kirschstein Predoctoral Fellowship F31NS118949. Rockwell P. Tang was supported by NIGMS T32GM145455. The authors acknowledge that data analysis was performed on the Shared Computing Cluster which is administered by Boston University's Research Computing Services. We thank the members of the Neurovascular Imaging Laboratory for helpful discussions.

## Data availability

Design blueprints, parts inventory, data acquisition and analysis software are available on github (https://github.com/NIL-NeuroScience/WidefieldImagingAnalysis); raw and processed data are available on Zenodo (for Figure 2, resting state: https://doi.org/10.5281/zenodo.10798934; for Figure 2 stimulus: https://doi.org/10.5281/zenodo.10798996; for Figure 3: https://doi.org/10.5281/zenodo.10798658; for Supplementary Figure 3: https://doi.org/10.5281/zenodo.10798091; for Supplementary Figure 6 resting state: https://doi.org/10.5281/zenodo.10805179; for Supplementary Figure 6 stimulus: https://doi.org/10.5281/zenodo.10805381).

## Author contributions

Patrick R. Doran: Investigation, Formal Analysis, Software, Visualization, Writing – original draft, Writing – review & editing; Natalie Fomin-Thunemann: Investigation, Writing – review & editing; Rockwell P. Tang: Investigation, Visualization, Writing – original draft, Writing – review & editing; Dora Balog: Software, Writing – review & editing; Bernhard Zimmermann, Kıvılcım Kılıç, Joel D. Herbert, Grace Chabbott, Bradley C. Rauscher, John X. Jiang: Resources, Writing – review & editing; Sreekanth Kura, Harrison P. Fisher: Software, Writing – review & editing; Sava Sakadzic, David A. Boas: Conceptualization, Writing – review & editing; Anna Devor: Conceptualization, Funding acquisition, Supervision, Writing – original draft, Writing – review & editing; Ichun Anderson Chen: Conceptualization, Methodology, Supervision, Writing – review & editing; Martin Thunemann: Conceptualization, Software, Supervision, Visualization, Writing – original draft, Writing – review & editing.

# Appendix

**Appendix A: Optimization of Δ[HbO] and Δ[HbR] estimation process for MATLAB using an explicit solution of HbR and HbO with measured reflectance at 525 nm and 625 nm.**

Concentration changes of deoxy- and oxyhemoglobin ($[HbR]$ and $[HbO]$) can be estimated using a system of linear equations (here, we use intensity measurements at two wavelengths (525 nm and 625 nm) and two unknowns ($[HbR]$ and $[HbO]$). For further discussion, see Ma et al. (2016).

The molar extinction coefficients $\varepsilon$ of Hb and HbO at 525 nm and 625 nm are known variables.

$$\Delta OD_{525} = \varepsilon_{525}^{HbO}\Delta[HbO] + \varepsilon_{525}^{HbR}\Delta[HbR] \tag{1}$$

$$\Delta OD_{625} = \varepsilon_{625}^{HbO}\Delta[HbO] + \varepsilon_{625}^{HbR}\Delta[HbR] \tag{2}$$

We estimate the optical density in every pixel for every time point t from the measured intensities $I_{525}^{t}$and $I_{625}^{t}$ as follows:

$$\Delta OD_{525} = \frac{-log\left(\frac{I_{525}^{t}}{I_{525}^{0}}\right)}{X_{525}} = -\frac{1}{X_{525}}\left(log(I_{525}^{t}) - log\left(I_{525}^{0}\right)\right) = \frac{log(I_{525}^{0})}{X_{525}} - \frac{log(I_{525}^{t})}{X_{525}} \tag{3}$$

$$\Delta OD_{625} = \frac{-log\left(\frac{I_{625}^{t}}{I_{625}^{0}}\right)}{X_{625}} = -\frac{1}{X_{625}}\left(log(I_{625}^{t}) - log\left(I_{625}^{0}\right)\right) = \frac{log(I_{625}^{0})}{X_{625}} - \frac{log(I_{625}^{t})}{X_{625}} \tag{4}$$

The pathlengths $X_{525}$ and $X_{625}$ are known variables; the “baseline” intensities $I_{525}^{0}$and $I_{625}^{0}$ are estimated using the temporal average of the intensities at the given pixel.

When we solve the equations (1) and (2) explicitly, combine them with equations (3) and (4), and combine all variables that are constant over space and/or time, we enable efficient (i.e., fast) approach for estimating $[Hb]$ and $[HbO]$.

To estimate $\Delta[HbO]$, we first solve equations 1 and 2 for $\Delta[Hb]$:

$$\Delta[Hb] = \frac{\Delta OD_{525}}{\varepsilon_{525}^{Hb}} - \frac{\varepsilon_{525}^{HbO}}{\varepsilon_{525}^{Hb}}\Delta[HbO], \tag{5.1}$$

$$\Delta[Hb] = \frac{\Delta OD_{625}}{\varepsilon_{625}^{Hb}} - \frac{\varepsilon_{625}^{HbO}}{\varepsilon_{625}^{Hb}}\Delta[HbO], \tag{5.2}$$

and combine equations 5.1 and 5.2:

$$\frac{\Delta OD_{525}}{\varepsilon_{525}^{Hb}} - \frac{\varepsilon_{525}^{HbO}}{\varepsilon_{525}^{Hb}}\Delta[HbO] = \frac{\Delta OD_{625}}{\varepsilon_{625}^{Hb}} - \frac{\varepsilon_{625}^{HbO}}{\varepsilon_{625}^{Hb}}\Delta[HbO]. \tag{5.3}$$

Then, we solve equation 5.3 for $\Delta[HbO]$:

$$\frac{\varepsilon_{625}^{HbO}}{\varepsilon_{625}^{Hb}}\Delta[HbO] - \frac{\varepsilon_{525}^{HbO}}{\varepsilon_{525}^{Hb}}\Delta[HbO] = \frac{\Delta OD_{625}}{\varepsilon_{625}^{Hb}} - \frac{\Delta OD_{525}}{\varepsilon_{525}^{Hb}}, \tag{5.4}$$

$$\left(\frac{\varepsilon_{625}^{HbO}\varepsilon_{525}^{Hb} - \varepsilon_{625}^{Hb}\varepsilon_{525}^{HbO}}{\varepsilon_{625}^{Hb}\varepsilon_{525}^{Hb}}\right)\Delta[HbO] = \frac{\Delta OD_{625}}{\varepsilon_{625}^{Hb}} - \frac{\Delta OD_{525}}{\varepsilon_{525}^{Hb}}, \tag{5.5}$$

$$\Delta[HbO] = \frac{1}{\varepsilon_{625}^{Hb}}\left(\frac{\varepsilon_{625}^{Hb}\varepsilon_{525}^{Hb}}{\varepsilon_{625}^{HbO}\varepsilon_{525}^{Hb} - \varepsilon_{625}^{Hb}\varepsilon_{525}^{HbO}}\right)\Delta OD_{625} - \frac{1}{\varepsilon_{525}^{Hb}}\left(\frac{\varepsilon_{625}^{Hb}\varepsilon_{525}^{Hb}}{\varepsilon_{625}^{HbO}\varepsilon_{525}^{Hb} - \varepsilon_{625}^{Hb}\varepsilon_{525}^{HbO}}\right)\Delta OD_{525}, \tag{5.6}$$

$$\Delta[HbO] = \left(\frac{\varepsilon_{525}^{Hb}}{\varepsilon_{625}^{HbO}\varepsilon_{525}^{Hb} - \varepsilon_{625}^{Hb}\varepsilon_{525}^{HbO}}\right)\Delta OD_{625} - \left(\frac{\varepsilon_{625}^{Hb}}{\varepsilon_{625}^{HbO}\varepsilon_{525}^{Hb} - \varepsilon_{625}^{Hb}\varepsilon_{525}^{HbO}}\right)\Delta OD_{525}. \tag{5.7}$$

Then, we combine all constant variables in equation 5.7 to define $C_{525}^{HbO}$ and $C_{625}^{HbO}$:

$$\Delta[HbO] = C_{625}^{HbO}\Delta OD_{625} - C_{525}^{HbO}\Delta OD_{525}. \tag{5.8}$$

Now, we insert the definition of $\Delta OD_{525}$ and $\Delta OD_{625}$ from equations 3 and 4:

$$\Delta[HbO] = C_{625}^{HbO}\left(\frac{log(I_{625}^{0})}{X_{625}} - \frac{log(I_{625}^{t})}{X_{625}}\right) - C_{525}^{HbO}\left(\frac{log(I_{525}^{0})}{X_{525}} - \frac{log(I_{525}^{t})}{X_{525}}\right) \tag{6.1}$$

and combine again all variables that are constant over time:

$$\Delta[HbO] = \frac{C_{625}^{HbO}}{X_{625}}log(I_{625}^{0}) - \frac{C_{625}^{HbO}}{X_{625}}log(I_{625}^{t}) - \frac{C_{525}^{HbO}}{X_{525}}log(I_{525}^{0}) + \frac{C_{525}^{HbO}}{X_{525}}log(I_{525}^{t}), \tag{6.2}$$

$$\Delta[HbO] = \frac{C_{625}^{HbO}}{X_{625}}log(I_{625}^{0}) - \frac{C_{525}^{HbO}}{X_{525}}log(I_{525}^{0}) + \frac{C_{525}^{HbO}}{X_{525}}log(I_{525}^{t}) - \frac{C_{625}^{HbO}}{X_{625}}log(I_{625}^{t}). \tag{6.3}$$

Finally, we combine all constant variables into three parameters $A_0^{HbO}$, $C_{525}^{HbO^*}$, and $C_{625}^{HbO^*}$:

$$\Delta[HbO] = A_0^{HbO} + C_{525}^{HbO^*}log(I_{525}^{t}) - C_{625}^{HbO^*}log(I_{625}^{t}) \tag{7.1}$$

with

$$C_{525}^{HbO^*} = \frac{C_{525}^{HbO}}{X_{525}} = \frac{1}{X_{525}}\left(\frac{\varepsilon_{625}^{Hb}}{\varepsilon_{625}^{HbO}\varepsilon_{525}^{Hb} - \varepsilon_{625}^{Hb}\varepsilon_{525}^{HbO}}\right), \tag{7.2}$$

$$C_{625}^{HbO^*} = \frac{C_{625}^{HbO}}{X_{625}} = \frac{1}{X_{625}}\left(\frac{\varepsilon_{525}^{Hb}}{\varepsilon_{625}^{HbO}\varepsilon_{525}^{Hb} - \varepsilon_{625}^{Hb}\varepsilon_{525}^{HbO}}\right), \text{ and} \tag{7.3}$$

$$A_0^{HbO} = \frac{C_{625}^{HbO}}{X_{625}} log\left(I_{625}^0\right) - \frac{C_{525}^{HbO}}{X_{525}} log\left(I_{525}^0\right) = C_{625}^{HbO^*} log\left(I_{625}^0\right) - C_{525}^{HbO^*} log\left(I_{525}^0\right) \tag{7.4}$$

*Note that $C_{525}^{HbO^*}$ and $C_{625}^{HbO^*}$ are invariant in time and space, while $A_0^{HbO}$ is only time-invariant – its value changes for every pixel.*

In the same way, we can estimate $[Hb]$. First, we solve equations 1 and 2 for $[HbO]$:

$$\Delta[HbO] = \frac{\Delta OD_{525}}{\varepsilon_{525}^{HbO}} - \frac{\varepsilon_{525}^{Hb}}{\varepsilon_{525}^{HbO}}\Delta[Hb], \tag{8.1}$$

$$\Delta[HbO] = \frac{\Delta OD_{625}}{\varepsilon_{625}^{HbO}} - \frac{\varepsilon_{625}^{Hb}}{\varepsilon_{625}^{HbO}}\Delta[Hb], \tag{8.2}$$

and combine equations 8.1 and 8.2:

$$\frac{\Delta OD_{525}}{\varepsilon_{525}^{HbO}} - \frac{\varepsilon_{525}^{Hb}}{\varepsilon_{525}^{HbO}}\Delta[Hb] = \frac{\Delta OD_{625}}{\varepsilon_{625}^{HbO}} - \frac{\varepsilon_{625}^{Hb}}{\varepsilon_{625}^{HbO}}\Delta[Hb]. \tag{8.3}$$

We solve equation 8.3 for Δ[Hb]:

$$\frac{\varepsilon_{625}^{Hb}}{\varepsilon_{625}^{HbO}}\Delta[Hb] - \frac{\varepsilon_{525}^{Hb}}{\varepsilon_{525}^{HbO}}\Delta[Hb] = \frac{\Delta OD_{625}}{\varepsilon_{625}^{HbO}} - \frac{\Delta OD_{525}}{\varepsilon_{525}^{HbO}}, \tag{8.4}$$

$$\left(\frac{\varepsilon_{625}^{Hb}\varepsilon_{525}^{HbO} - \varepsilon_{625}^{HbO}\varepsilon_{525}^{Hb}}{\varepsilon_{625}^{HbO}\varepsilon_{525}^{HbO}}\right)\Delta[Hb] = \frac{\Delta OD_{625}}{\varepsilon_{625}^{HbO}} - \frac{\Delta OD_{525}}{\varepsilon_{525}^{HbO}}, \tag{8.5}$$

$$\Delta[Hb] = \frac{1}{\varepsilon_{625}^{HbO}}\left(\frac{\varepsilon_{625}^{HbO}\varepsilon_{525}^{HbO}}{\varepsilon_{625}^{Hb}\varepsilon_{525}^{HbO} - \varepsilon_{625}^{HbO}\varepsilon_{525}^{Hb}}\right)\Delta OD_{625} - \frac{1}{\varepsilon_{525}^{HbO}}\left(\frac{\varepsilon_{625}^{HbO}\varepsilon_{525}^{HbO}}{\varepsilon_{625}^{Hb}\varepsilon_{525}^{HbO} - \varepsilon_{625}^{HbO}\varepsilon_{525}^{Hb}}\right)\Delta OD_{525}, \tag{8.6}$$

$$\Delta[Hb] = \left(\frac{\varepsilon_{525}^{HbO}}{\varepsilon_{625}^{Hb}\varepsilon_{525}^{HbO} - \varepsilon_{625}^{HbO}\varepsilon_{525}^{Hb}}\right)\Delta OD_{625} - \left(\frac{\varepsilon_{625}^{HbO}}{\varepsilon_{625}^{Hb}\varepsilon_{525}^{HbO} - \varepsilon_{625}^{HbO}\varepsilon_{525}^{Hb}}\right)\Delta OD_{525}. \tag{8.7}$$

We combine all constant variables in equation 8.7 to define $C_{525}^{Hb}$ and $C_{625}^{Hb}$

$$\Delta[Hb] = C_{625}^{Hb}\Delta OD_{625} - C_{525}^{Hb}\Delta OD_{525} \tag{8.8}$$

and insert the definition of $\Delta OD_{525}$ and $\Delta OD_{625}$ from equations 3 and 4:

$$\Delta[Hb] = C_{625}^{Hb}\left(\frac{log\left(I_{625}^0\right)}{X_{625}} - \frac{log\left(I_{625}^t\right)}{X_{625}}\right) - C_{525}^{Hb}\left(\frac{log\left(I_{525}^0\right)}{X_{525}} - \frac{log\left(I_{525}^t\right)}{X_{525}}\right). \tag{9.1}$$

Then, we combine again all variables that are constant over time:

$$\Delta[Hb] = \frac{C_{625}^{Hb}}{X_{625}} log\left(I_{625}^{0}\right) - \frac{C_{625}^{Hb}}{X_{625}} log(I_{625}^{t}) - \frac{C_{525}^{Hb}}{X_{525}} log\left(I_{525}^{0}\right) + \frac{C_{525}^{Hb}}{X_{525}} log(I_{525}^{t}), \tag{9.2}$$

$$\Delta[Hb] = \frac{C_{625}^{Hb}}{X_{625}} log\left(I_{625}^{0}\right) - \frac{C_{525}^{Hb}}{X_{525}} log\left(I_{525}^{0}\right) - \frac{C_{625}^{Hb}}{X_{625}} log(I_{625}^{t}) + \frac{C_{525}^{Hb}}{X_{525}} log(I_{525}^{t}). \tag{9.3}$$

Finally, we combine all constant variables into three parameters $A_0^{Hb}$, ${C_{525}^{Hb}}^*$, and ${C_{625}^{Hb}}^*$:

$$\Delta[Hb] = A_0^{Hb} + {C_{525}^{Hb}}^* log(I_{525}^{t}) - {C_{625}^{Hb}}^* log(I_{625}^{t}) \tag{10.1}$$

with

$${C_{625}^{Hb}}^* = \frac{C_{625}^{Hb}}{X_{625}} = \frac{1}{X_{625}}\left(\frac{\varepsilon_{525}^{HbO}}{\varepsilon_{625}^{Hb}\varepsilon_{525}^{HbO} - \varepsilon_{625}^{HbO}\varepsilon_{525}^{Hb}}\right), \tag{10.2}$$

$${C_{525}^{Hb}}^* = \frac{C_{525}^{Hb}}{X_{525}} = \frac{1}{X_{525}}\left(\frac{\varepsilon_{625}^{HbO}}{\varepsilon_{625}^{Hb}\varepsilon_{525}^{HbO} - \varepsilon_{625}^{HbO}\varepsilon_{525}^{Hb}}\right), \text{ and} \tag{10.3}$$

$$A_0^{Hb} = \frac{C_{625}^{Hb}}{X_{625}} log\left(I_{625}^{0}\right) - \frac{C_{525}^{Hb}}{X_{525}} log\left(I_{525}^{0}\right) = {C_{625}^{Hb}}^* log\left(I_{625}^{0}\right) - {C_{525}^{Hb}}^* log\left(I_{525}^{0}\right) \tag{10.4}$$

*Note that ${C_{525}^{Hb}}^*$ and ${C_{625}^{Hb}}^*$ are invariant in time and space, while $A_0^{Hb}$ is only time-invariant – its value changes for every pixel.*

<u>*MATLAB implementation:*</u>

(1) Calculate ${C_{525}^{Hb}}^*$, ${C_{625}^{Hb}}^*$, ${C_{525}^{HbO}}^*$, and ${C_{625}^{HbO}}^*$ [dim: 1]
(2) Calculate $log(I_{525}^{t})$ and $log(I_{625}^{t})$ [dim: WxHxT]
(3) Calculate $log\left(I_{525}^{0}\right)$ and $log\left(I_{625}^{0}\right)$ [dim: WxH]
(4) Calculate $A_0^{Hb}$ and $A_0^{HbO}$ [dim: WxH]
(5) Estimate ${C_{525}^{Hb}}^* log(I_{525}^{t})$, ${C_{625}^{Hb}}^* log(I_{625}^{t})$ [dim: WxHxT]
(6) Combine $\Delta[Hb] = A_0^{Hb} + {C_{525}^{Hb}}^* log(I_{525}^{t}) - {C_{625}^{Hb}}^* log(I_{625}^{t})$ [dim: WxHxT]
(7) Estimate ${C_{525}^{HbO}}^* log(I_{525}^{t})$, and ${C_{625}^{HbO}}^* log(I_{625}^{t})$ [dim: WxHxT]
(8) Combine $\Delta[HbO] = A_0^{HbO} + {C_{525}^{HbO}}^* log(I_{525}^{t}) - {C_{625}^{HbO}}^* log(I_{625}^{t})$ [dim: WxHxT]

## Appendix B: Evaluation of potential crosstalk between EGFP- and mApple-derived fluorophores

*Part I: in vitro calibration with purified EGFP and mApple fluorescent proteins*

We performed fluorescence measurements of purified EGFP and mApple that were excited at 475 nm and 565 nm using series of increasing exposure times and optical powers. For further evaluation, we calculated the radiant energy $E$ for each measurement as the product of illumination power, estimated from the LED current using a separately measured power calibration curve, and exposure time.

Then, we defined the illumination ratio $R$ for EGFP and mApple as radiant energy at off-peak illumination divided by radiant energy at on-peak illumination combining different illumination conditions for on- and off-peak excitation into a single variable:

$$R_{EGFP} = \left(P_1^{565\,nm} \times t_1^{565\,nm}\right)/(P_1^{470\,nm} \times t_1^{470\,nm}) = E_1^{565\,nm}/E_2^{470\,nm} \text{ and} \quad (1)$$

$$R_{mApple} = (P_1^{470\,nm} \times t_1^{470\,nm})/\left(P_1^{565\,nm} \times t_1^{565\,nm}\right) = E_1^{470\,nm}/E_2^{565\,nm}. \quad (2)$$

Note that every illumination ratio can be achieved by different combinations of optical powers and exposure times. This means that pairs of fluorescence measurements are performed with different combinations of optical power and exposure time for off- and on-peak excitation but match the chosen illumination ratio. The corresponding individual on- and off-peak fluorescence intensities have different values. We define their ratio, measured at a certain LED power $P_1$ and exposure time $t_1$ at off-peak excitation relative to the fluorescence intensity at a certain LED power $P_2$ and exposure time $t_2$ at on-peak excitation for each fluorophore as crosstalk ratio $\mathrm{C}$ for EGFP and mApple as

$$C_{EGFP} = F_{EGFP}^{565\,nm}\left(P_1^{565\,nm}, t_1^{565\,nm}\right)/F_{EGFP}^{470\,nm}(P_2^{470\,nm}, t_2^{470\,nm}) \text{ and} \quad (3)$$

$$C_{mApple} = F_{EGFP}^{470\,nm}(P_1^{470\,nm}, t_1^{470\,nm})/F_{EGFP}^{565\,nm}\left(P_2^{565\,nm}, t_2^{565\,nm}\right). \quad (4)$$

We again substitute LED power and exposure time by radiant energy $E$ :

$$C_{EGFP} = F_{EGFP}^{565\,nm}\left(E_1^{565\,nm}\right)/F_{EGFP}^{470\,nm}(E_2^{470\,nm}) \text{ and} \quad (5)$$

$$C_{mApple} = F_{mApple}^{470\,nm}(E_1^{470\,nm})/F_{mApple}^{565\,nm}\left(E_2^{565\,nm}\right). \quad (6)$$

To estimate the crosstalk ratio $\mathrm{C}$, we chose 20 pairs of measurements matching a given illumination ratio $R$. The pairs of fluorescence intensities from off-peak excitation versus on-peak

excitation, when plotted against each other, follow a linear relationship (**Supplementary Figure 2C, D**), which is expected given the underlying linear relationship between fluorescence intensity and radiant energy (shown in **Supplementary Figure 2A, B**). Accordingly, we can estimate the crosstalk ratio $\mathrm{C}$ from the slope of the linear fit between fluorescence from off- and on-peak excitation for the 20 pairs of values for each given illumination ratio (**Supplementary Figure 2C, D**). Finally, for each fluorophore we plot the crosstalk ratio $\mathrm{C}$ versus illumination ratio $R$ for EGFP and mApple (i.e., $C_{EGFP}$ versus $E^{565\,nm}/E^{470\,nm}$ and $C_{mApple}$ versus $E^{470\,nm}/E^{565\,nm}$ ; **Supplementary Figure 2E**). In the resulting graph, a small value of $R$ indicates weak off-peak excitation compared to on-peak excitation, and the resulting crosstalk ratio $\mathrm{C}$ is small. For increasing values of $R$, off-peak excitation becomes increasingly stronger compared to on-peak excitation leading to a higher crosstalk ratio $\mathrm{C}$. Given that EGFP shows only very weak off-peak excitation at 565 nm, its crosstalk ratio $\mathrm{C}$ increases only modestly with $\mathrm{R}$. In contrast, as mApple is more efficiently excited off-peak at 470 nm, the crosstalk ratio $\mathrm{C}$ rises faster with increasing $R$.

*Part II: in vivo correction of jRGECO1a crosstalk upon 470-nm excitation in GRAB$_{ACh3.0}$ and jRGECO1a-expressing animals*

In experiments with jRGECO1a- and GRAB$_{ACh3.0}$-expressing mice (**Figure 2**), the used LED powers and exposure times for fluorescence excitation at 470 and 565 nm define a range of illumination ratios. Based on the *in-vitro* calibration with EGFP and mApple, we estimated that for EGFP-derived GRAB$_{ACh3.0}$, <1% of its fluorescence present at 470-nm excitation contributes to fluorescence measured at 565-nm excitation, while for mApple-derived jRGECO1a, 3-9% of its fluorescence present at 565-nm excitation contributes to fluorescence measured at 470-nm excitation (highlighted areas in **Supplementary Figure 2E)**.

Calibration of the crosstalk ratio $\mathrm{C}$ enables us to estimate the level of fluorescence present at 470-nm excitation due to off-peak excitation of jRGECO1a for a given combination of illumination power and exposure times, i.e., radiant energies $E_1$ and $E_2$ :

$$F_{mApple}^{470\,nm}(E_1^{470\,nm}) = C_{mApple}\left(E_1^{470\,nm}, E_2^{565\,nm}\right) \times F_{mApple}^{565\,nm}\left(E_2^{565\,nm}\right) \quad (7)$$

We assume here that fluorescence measured at 565 nm is solely due to jRGECO1a fluorescence with negligible contribution from GRAB$_{ACh3.0}$, given the minor (<1%) contribution of EGFP fluorescence at 565 nm excitation. This enables us to define the following correction term to remove jRGECO1a crosstalk from fluorescence measured at 470-nm excitation:

$$F_{corrected}^{470\,nm}(E_1^{470\,nm}) = F_{measured}^{470\,nm}(E_1^{470\,nm}) - F_{mApple}^{470\,nm}(E_1^{470\,nm}), \text{ or} \quad (8)$$

684 $$F_{corrected}^{470\,nm}(E_1^{470\,nm}) = F_{measured}^{470\,nm}(E_1^{470\,nm}) - C_{mApple}\left(E_1^{470\,nm}, E_2^{565\,nm}\right) \times F_{mApple}^{565\,nm}\left(E_2^{565\,nm}\right). \quad (9)$$

685 To apply this correction approach based on *in-vitro* determined crosstalk ratios $C$ to *in-vivo* data,
686 we make the following assumptions: (a) fluorescence acquired at 565 nm is solely caused by
687 jRGECO1a and (b) dynamic changes in jRGECO1a fluorescence between consecutive
688 acquisition of images at 470-nm and 565-nm excitation are negligible. Further, we do not consider
689 wavelength-dependent absorption of light for fluorescence excitation and emission through
690 hemoglobin. Incorporating [HbO] and [HbR] estimates into the correction would result in
691 combining measurements from all four wavelengths to correct for crosstalk in fluorescence
692 measurements at 470-nm excitation, potentially confounding this measurement, i.e., $GRAB_{ACh3.0}$
693 fluorescence, by the sum of measurement noise from all measured channels.

694 To verify that the degree of in-vivo crosstalk matches our in-vitro estimation, following equation
695 (9), we assume that we can estimate the "true" $GRAB_{ACh3.0}$ signal by subtracting a proportion C
696 of the 565-nm fluorescence image intensity from the 470-nm fluorescence image on a pixel-by-
697 pixel and frame-by-frame basis. Here, we subtracted on a frame-by-frame three different crosstalk
698 ratios (we tested C=0, 3%, 5%, 10%) and estimated the cross-correlation of the resulting,
699 corrected $F_{470}$ timeseries with the $F_{565}$ timeseries (**Supplementary Figure 3**). For C of 5% and
700 10%, we observe clear, negative zero-lag cross-correlation indicative for overcorrection. This
701 result suggests that the degree of crosstalk established under in vitro conditions is a reasonable
702 estimate of the crosstalk we observe in vivo. Based on this evaluation, we suggest that under the
703 illumination conditions for in vivo imaging used here, the benefits of spectral crosstalk correction
704 are minimal. Therefore, we did not perform crosstalk correction for the data shown in **Figure 2**.

705 However, it is possible that levels of crosstalk increase, particularly when fluorescence from on-
706 peak excitation of one fluorophore approaches levels of the other fluorophore due to off-peak
707 excitation at the same wavelength. First, this could happen due to low expression of one
708 fluorescent indicator versus the other. Here, using AAV delivery into newborn pups, we achieved
709 relatively high levels of $GRAB_{ACh3.0}$, diminishing the potential effect of jRGECO1a crosstalk on
710 $GRAB_{ACh3.0}$ measurements. Second, this situation could also arise when one fluorescent indicator
711 has low levels of basal fluorescence in virtual absence of its analyte, i.e., acetylcholine for
712 $GRAB_{ACh3.0}$ in this study. When ACh levels are low (low $GRAB_{ACh3.0}$ fluorescence) and neuronal
713 calcium levels are high (high jRGECO1a fluorescence), the measurement at 470-nm excitation
714 could potentially show higher contribution from jRGECO1a fluorescence compared to periods
715 where ACh levels are high. To further address and quantify this effect, however, is very difficult

716 with the used animals under the given imaging conditions as jRGECO1a and $GRAB_{ACh3.0}$ signals
717 show high correlation due to their underlying physiological covariance.

718

## References


Abdelfattah, A. S., S. Ahuja, T. Akkin, S. R. Allu, J. Brake, D. A. Boas, E. M. Buckley, R. E. Campbell, A. I. Chen, X. Cheng, T. Cizmar, I. Costantini, M. De Vittorio, A. Devor, P. R. Doran, M. El Khatib, V. Emiliani, N. Fomin-Thunemann, Y. Fainman, T. Fernandez-Alfonso, C. G. L. Ferri, A. Gilad, X. Han, A. Harris, E. M. C. Hillman, U. Hochgeschwender, M. G. Holt, N. Ji, K. Kilic, E. M. R. Lake, L. Li, T. Li, P. Machler, E. W. Miller, R. C. Mesquita, K. Nadella, U. V. Nagerl, Y. Nasu, A. Nimmerjahn, P. Ondrackova, F. S. Pavone, C. Perez Campos, D. S. Peterka, F. Pisano, F. Pisanello, F. Puppo, B. L. Sabatini, S. Sadegh, S. Sakadzic, S. Shoham, S. N. Shroff, R. A. Silver, R. R. Sims, S. L. Smith, V. J. Srinivasan, M. Thunemann, L. Tian, L. Tian, T. Troxler, A. Valera, A. Vaziri, S. A. Vinogradov, F. Vitale, L. V. Wang, H. Uhlirova, C. Xu, C. Yang, M. H. Yang, G. Yellen, O. Yizhar and Y. Zhao (2022). "Neurophotonic tools for microscopic measurements and manipulation: status report." Neurophotonics **9**(Suppl 1): 013001.

Allen, W. E., I. V. Kauvar, M. Z. Chen, E. B. Richman, S. J. Yang, K. Chan, V. Gradinaru, B. E. Deverman, L. Luo and K. Deisseroth (2017). "Global Representations of Goal-Directed Behavior in Distinct Cell Types of Mouse Neocortex." Neuron **94**(4): 891-907 e896.

Bouchard, M. B., B. R. Chen, S. A. Burgess and E. M. Hillman (2009). "Ultra-fast multispectral optical imaging of cortical oxygenation, blood flow, and intracellular calcium dynamics." Opt Express **17**(18): 15670-15678.

Cardin, J. A., M. C. Crair and M. J. Higley (2020). "Mesoscopic Imaging: Shining a Wide Light on Large-Scale Neural Dynamics." Neuron **108**(1): 33-43.

Celebi, I., M. Aslan and M. S. Unlu (2023). "A spatially uniform illumination source for widefield multi-spectral optical microscopy." PLoS One **18**(10): e0286988.

Couto, J., S. Musall, X. R. Sun, A. Khanal, S. Gluf, S. Saxena, I. Kinsella, T. Abe, J. P. Cunningham, L. Paninski and A. K. Churchland (2021). "Chronic, cortex-wide imaging of specific cell populations during behavior." Nat Protoc **16**(7): 3241-3263.

Cramer, S. W., R. E. Carter, J. D. Aronson, S. B. Kodandaramaiah, T. J. Ebner and C. C. Chen (2021). "Through the looking glass: A review of cranial window technology for optical access to the brain." J Neurosci Methods **354**: 109100.

Dana, H., B. Mohar, Y. Sun, S. Narayan, A. Gordus, J. P. Hasseman, G. Tsegaye, G. T. Holt, A. Hu, D. Walpita, R. Patel, J. J. Macklin, C. I. Bargmann, M. B. Ahrens, E. R. Schreiter, V. Jayaraman, L. L. Looger, K. Svoboda and D. S. Kim (2016). "Sensitive red protein calcium indicators for imaging neural activity." Elife **5**.

Dana, H., Y. Sun, B. Mohar, B. K. Hulse, A. M. Kerlin, J. P. Hasseman, G. Tsegaye, A. Tsang, A. Wong, R. Patel, J. J. Macklin, Y. Chen, A. Konnerth, V. Jayaraman, L. L. Looger, E. R. Schreiter, K. Svoboda and D. S. Kim (2019). "High-performance calcium sensors for imaging activity in neuronal populations and microcompartments." Nat Methods **16**(7): 649-657.

Echagarruga, C. T., K. W. Gheres, J. N. Norwood and P. J. Drew (2020). "nNOS-expressing interneurons control basal and behaviorally evoked arterial dilation in somatosensory cortex of mice." Elife **9**.

Gilad, A., Y. Gallero-Salas, D. Groos and F. Helmchen (2018). "Behavioral Strategy Determines Frontal or Posterior Location of Short-Term Memory in Neocortex." Neuron **99**(4): 814-828 e817.

Gribizis, A., X. Ge, T. L. Daigle, J. B. Ackman, H. Zeng, D. Lee and M. C. Crair (2019). "Visual Cortex Gains Independence from Peripheral Drive before Eye Opening." Neuron **104**(4): 711-723 e713.

Harrison, T. C., A. Sigler and T. H. Murphy (2009). "Simple and cost-effective hardware and software for functional brain mapping using intrinsic optical signal imaging." J Neurosci Methods **182**(2): 211-218.

Higley, M. J. and J. A. Cardin (2022). "Spatiotemporal dynamics in large-scale cortical networks." Curr Opin Neurobiol **77**: 102627.

Jacobs, E. A. K., N. A. Steinmetz, A. J. Peters, M. Carandini and K. D. Harris (2020). "Cortical State Fluctuations during Sensory Decision Making." Curr Biol **30**(24): 4944-4955 e4947.

Jing, M., Y. Li, J. Zeng, P. Huang, M. Skirzewski, O. Kljakic, W. Peng, T. Qian, K. Tan, J. Zou, S. Trinh, R. Wu, S. Zhang, S. Pan, S. A. Hires, M. Xu, H. Li, L. M. Saksida, V. F. Prado, T. J. Bussey, M. A. M. Prado, L. Chen, H. Cheng and Y. Li (2020). "An optimized acetylcholine sensor for monitoring in vivo cholinergic activity." Nat Methods **17**(11): 1139-1146.

Joshi, S., Y. Li, R. M. Kalwani and J. I. Gold (2016). "Relationships between Pupil Diameter and Neuronal Activity in the Locus Coeruleus, Colliculi, and Cingulate Cortex." Neuron **89**(1): 221-234.

Kilic, K., M. Desjardins, J. Tang, M. Thunemann, S. Sunil, S. E. Erdener, D. D. Postnov, D. A. Boas and A. Devor (2020). "Chronic Cranial Windows for Long Term Multimodal Neurovascular Imaging in Mice." Front Physiol **11**: 612678.

Kim, T. H., Y. Zhang, J. Lecoq, J. C. Jung, J. Li, H. Zeng, C. M. Niell and M. J. Schnitzer (2016). "Long-Term Optical Access to an Estimated One Million Neurons in the Live Mouse Cortex." Cell Rep **17**(12): 3385-3394.

Lake, E. M. R., X. Ge, X. Shen, P. Herman, F. Hyder, J. A. Cardin, M. J. Higley, D. Scheinost, X. Papademetris, M. C. Crair and R. T. Constable (2020). "Simultaneous cortex-wide fluorescence Ca(2+) imaging and whole-brain fMRI." Nat Methods **17**(12): 1262-1271.

Lerner, T. N., C. Shilyansky, T. J. Davidson, K. E. Evans, K. T. Beier, K. A. Zalocusky, A. K. Crow, R. C. Malenka, L. Luo, R. Tomer and K. Deisseroth (2015). "Intact-Brain Analyses Reveal Distinct Information Carried by SNc Dopamine Subcircuits." Cell **162**(3): 635-647.

Lin, M. Z. and M. J. Schnitzer (2016). "Genetically encoded indicators of neuronal activity." Nat Neurosci **19**(9): 1142-1153.

Lohani, S., A. H. Moberly, H. Benisty, B. Landa, M. Jing, Y. Li, M. J. Higley and J. A. Cardin (2022). "Spatiotemporally heterogeneous coordination of cholinergic and neocortical activity." Nat Neurosci **25**(12): 1706-1713.

Lu, X., Y. Wang, Z. Liu, Y. Gou, D. Jaeger and F. St-Pierre (2023). "Widefield imaging of rapid pan-cortical voltage dynamics with an indicator evolved for one-photon microscopy." Nat Commun **14**(1): 6423.

Ma, Y., M. A. Shaik, S. H. Kim, M. G. Kozberg, D. N. Thibodeaux, H. T. Zhao, H. Yu and E. M. Hillman (2016a). "Wide-field optical mapping of neural activity and brain haemodynamics: considerations and novel approaches." Philos Trans R Soc Lond B Biol Sci **371**(1705): 20150360.

Ma, Y., M. A. Shaik, M. G. Kozberg, S. H. Kim, J. P. Portes, D. Timerman and E. M. Hillman (2016b). "Resting-state hemodynamics are spatiotemporally coupled to synchronized and symmetric neural activity in excitatory neurons." Proc Natl Acad Sci U S A **113**(52): E8463-E8471.

MacDowell, C. J. and T. J. Buschman (2020). "Low-Dimensional Spatiotemporal Dynamics Underlie Cortex-wide Neural Activity." Curr Biol **30**(14): 2665-2680 e2668.

Machler, P., T. Broggini, C. Mateo, M. Thunemann, N. Fomin-Thunemann, P. R. Doran, I. Sencan, K. Kilic, M. Desjardins, H. Uhlirova, M. A. Yaseen, D. A. Boas, A. A. Linninger, M. Vergassola, X. Yu, L. D. Lewis, J. R. Polimeni, B. R. Rosen, S. Sakadzic, R. B. Buxton, M. Lauritzen, D. Kleinfeld and A. Devor (2021). "A Suite of Neurophotonic Tools to Underpin the Contribution of Internal Brain States in fMRI." Curr Opin Biomed Eng **18**: 100273.

Makino, H., C. Ren, H. Liu, A. N. Kim, N. Kondapaneni, X. Liu, D. Kuzum and T. Komiyama (2017). "Transformation of Cortex-wide Emergent Properties during Motor Learning." Neuron **94**(4): 880-890 e888.

Matsui, T., T. Murakami and K. Ohki (2016). "Transient neuronal coactivations embedded in globally propagating waves underlie resting-state functional connectivity." Proc Natl Acad Sci U S A **113**(23): 6556-6561.

Mitra, A., A. Kraft, P. Wright, B. Acland, A. Z. Snyder, Z. Rosenthal, L. Czerniewski, A. Bauer, L. Snyder, J. Culver, J. M. Lee and M. E. Raichle (2018). "Spontaneous Infra-slow Brain Activity Has Unique Spatiotemporal Dynamics and Laminar Structure." Neuron **98**(2): 297-305 e296.

Mohajerani, M. H., A. W. Chan, M. Mohsenvand, J. LeDue, R. Liu, D. A. McVea, J. D. Boyd, Y. T. Wang, M. Reimers and T. H. Murphy (2013). "Spontaneous cortical activity alternates between motifs defined by regional axonal projections." Nat Neurosci **16**(10): 1426-1435.

Musall, S., M. T. Kaufman, A. L. Juavinett, S. Gluf and A. K. Churchland (2019). "Single-trial neural dynamics are dominated by richly varied movements." Nat Neurosci **22**(10): 1677-1686.

Nietz, A. K., M. L. Streng, L. S. Popa, R. E. Carter, E. B. Flaherty, J. D. Aronson and T. J. Ebner (2023). "To be and not to be: wide-field Ca2+ imaging reveals neocortical functional segmentation combines stability and flexibility." Cereb Cortex **33**(11): 6543-6558.

Padawer-Curry, J. A., R. M. Bowen, A. Jarang, X. Wang, J.-M. Lee and A. Q. Bauer (2023). Wide-Field Optical Imaging in Mouse Models of Ischemic Stroke. Neural Repair: Methods and Protocols. V. T. Karamyan and A. M. Stowe. New York, NY, Springer US**:** 113-151.

Park, K., A. C. Liyanage, A. P. Koretsky, Y. Pan and C. Du (2020). "Optical imaging of stimulation-evoked cortical activity using GCaMP6f and jRGECO1a." Quantitative Imaging in Medicine and Surgery **11**(3): 998-1009.

Peters, A. J., J. M. J. Fabre, N. A. Steinmetz, K. D. Harris and M. Carandini (2021). "Striatal activity topographically reflects cortical activity." Nature **591**(7850): 420-425.

Prahl, S. (1999). "Optical Absorption of Hemoglobin." Retrieved 11/3/2023, 2023, from https://omlc.org/spectra/hemoglobin/.

Qian, Y., D. M. O. Cosio, K. D. Piatkevich, S. Aufmkolk, W. C. Su, O. T. Celiker, A. Schohl, M. H. Murdock, A. Aggarwal, Y. F. Chang, P. W. Wiseman, E. S. Ruthazer, E. S. Boyden and R. E. Campbell (2020). "Improved genetically encoded near-infrared fluorescent calcium ion indicators for in vivo imaging." PLoS Biol **18**(11): e3000965.

Raut, R. V., Z. P. Rosenthal, X. Wang, H. Miao, Z. Zhang, J. M. Lee, M. E. Raichle, A. Q. Bauer, S. L. Brunton, B. W. Brunton and J. N. Kutz (2023). "Arousal as a universal embedding for spatiotemporal brain dynamics." bioRxiv: 2023.2011.2006.565918.

Reimer, J., M. J. McGinley, Y. Liu, C. Rodenkirch, Q. Wang, D. A. McCormick and A. S. Tolias (2016). "Pupil fluctuations track rapid changes in adrenergic and cholinergic activity in cortex." Nat Commun **7**: 13289.

Shahsavarani, S., D. N. Thibodeaux, W. Xu, S. H. Kim, F. Lodgher, C. Nwokeabia, M. Cambareri, A. J. Yagielski, H. T. Zhao, D. A. Handwerker, J. Gonzalez-Castillo, P. A. Bandettini and E. M. C. Hillman (2023). "Cortex-wide neural dynamics predict behavioral states and provide a neural basis for resting-state dynamic functional connectivity." Cell Rep **42**(6): 112527.

Silasi, G., D. Xiao, M. P. Vanni, A. C. Chen and T. H. Murphy (2016). "Intact skull chronic windows for mesoscopic wide-field imaging in awake mice." J Neurosci Methods **267**: 141-149.

Sunil, S., J. Jiang, S. Shah, S. Kura, K. Kilic, S. E. Erdener, C. Ayata, A. Devor and D. A. Boas (2023). "Neurovascular coupling is preserved in chronic stroke recovery after targeted photothrombosis." Neuroimage Clin **38**: 103377.

Thunemann, M., Y. Lu, X. Liu, K. Kilic, M. Desjardins, M. Vandenberghe, S. Sadegh, P. A. Saisan, Q. Cheng, K. L. Weldy, H. Lyu, S. Djurovic, O. A. Andreassen, A. M. Dale, A. Devor and D. Kuzum

(2018). "Deep 2-photon imaging and artifact-free optogenetics through transparent graphene microelectrode arrays." Nat Commun **9**(1): 2035.

Uhlirova, H., K. Kilic, P. Tian, S. Sakadzic, L. Gagnon, M. Thunemann, M. Desjardins, P. A. Saisan, K. Nizar, M. A. Yaseen, D. J. Hagler, Jr., M. Vandenberghe, S. Djurovic, O. A. Andreassen, G. A. Silva, E. Masliah, D. Kleinfeld, S. Vinogradov, R. B. Buxton, G. T. Einevoll, D. A. Boas, A. M. Dale and A. Devor (2016a). "The roadmap for estimation of cell-type-specific neuronal activity from non-invasive measurements." Philos Trans R Soc Lond B Biol Sci **371**(1705).

Uhlirova, H., K. Kilic, P. Tian, M. Thunemann, M. Desjardins, P. A. Saisan, S. Sakadzic, T. V. Ness, C. Mateo, Q. Cheng, K. L. Weldy, F. Razoux, M. Vandenberghe, J. A. Cremonesi, C. G. Ferri, K. Nizar, V. B. Sridhar, T. C. Steed, M. Abashin, Y. Fainman, E. Masliah, S. Djurovic, O. A. Andreassen, G. A. Silva, D. A. Boas, D. Kleinfeld, R. B. Buxton, G. T. Einevoll, A. M. Dale and A. Devor (2016b). "Cell type specificity of neurovascular coupling in cerebral cortex." Elife **5**.

Valley, M. T., M. G. Moore, J. Zhuang, N. Mesa, D. Castelli, D. Sullivan, M. Reimers and J. Waters (2020). "Separation of hemodynamic signals from GCaMP fluorescence measured with wide-field imaging." J Neurophysiol **123**(1): 356-366.

Vanni, M. P., A. W. Chan, M. Balbi, G. Silasi and T. H. Murphy (2017). "Mesoscale Mapping of Mouse Cortex Reveals Frequency-Dependent Cycling between Distinct Macroscale Functional Modules." J Neurosci **37**(31): 7513-7533.

Vinck, M., R. Batista-Brito, U. Knoblich and J. A. Cardin (2015). "Arousal and locomotion make distinct contributions to cortical activity patterns and visual encoding." Neuron **86**(3): 740-754.

Wang, Q., S. L. Ding, Y. Li, J. Royall, D. Feng, P. Lesnar, N. Graddis, M. Naeemi, B. Facer, A. Ho, T. Dolbeare, B. Blanchard, N. Dee, W. Wakeman, K. E. Hirokawa, A. Szafer, S. M. Sunkin, S. W. Oh, A. Bernard, J. W. Phillips, M. Hawrylycz, C. Koch, H. Zeng, J. A. Harris and L. Ng (2020). "The Allen Mouse Brain Common Coordinate Framework: A 3D Reference Atlas." Cell **181**(4): 936-953 e920.

Wang, X., A. Bice, J. Padawer-Curry, Z. Rosenthal, J.-M. Lee and A. Bauer (2022). Dual fluorophore imaging combined with optical intrinsic signal to acquire neural, metabolic and hemodynamic activity, SPIE.

Wekselblatt, J. B., E. D. Flister, D. M. Piscopo and C. M. Niell (2016). "Large-scale imaging of cortical dynamics during sensory perception and behavior." J Neurophysiol **115**(6): 2852-2866.

White, B. R., A. Q. Bauer, A. Z. Snyder, B. L. Schlaggar, J. M. Lee and J. P. Culver (2011). "Imaging of functional connectivity in the mouse brain." PLoS One **6**(1): e16322.

Wright, P. W., L. M. Brier, A. Q. Bauer, G. A. Baxter, A. W. Kraft, M. D. Reisman, A. R. Bice, A. Z. Snyder, J. M. Lee and J. P. Culver (2017). "Functional connectivity structure of cortical calcium dynamics in anesthetized and awake mice." PLoS One **12**(10): e0185759.

Yang, F., M. Y. Shalaginov, H. Lin, S. S. An, A. Agarwal, H. L. Zhang, C. Rivero-Baleine, T. Gu and J. J. Hu (2023). "Wide field-of-view metalens: a tutorial." Advanced Photonics **5**(3): 033001.

Zatka-Haas, P., N. A. Steinmetz, M. Carandini and K. D. Harris (2021). "Sensory coding and the causal impact of mouse cortex in a visual decision." Elife **10**: e63163.

Zhao, Y., S. Araki, J. Wu, T. Teramoto, Y. F. Chang, M. Nakano, A. S. Abdelfattah, M. Fujiwara, T. Ishihara, T. Nagai and R. E. Campbell (2011). "An expanded palette of genetically encoded Ca(2)(+) indicators." Science **333**(6051): 1888-1891.

901 ## Figure Legends

902 **Figure 1. Schematics of the wide field imaging system and fluorescence and reflectance**
903 **spectra. A.** A single sCMOS camera is used to measure emission of green and red fluorophores
904 and two hemoglobin absorption wavelengths. A 565-nm LED excites mApple-based jRGECO1a
905 and a 470-nm LED excites EGFP-based $GRAB_{ACh3.0}$; both LEDs are filtered through excitation
906 filters. The main dichroic mirror reflects excitation light towards a 45°-mirror and then a 0.63×
907 objective lens to focus the excitation light onto the sample. Below the objective lens is the
908 reflectance illumination ring (RIR) further detailed in panel B. An aluminum hemisphere between
909 the RIR and the sample surface internally reflects the 525- and 625-nm LEDs for diffuse
910 illumination prevents specular reflections and illumination light from reaching the animal's eyes.
911 Fluorescence emission and reflectance pass the main dichroic and the detection filter before
912 being focused by a tube lens to the camera. **B.** Cross-section of the reflectance illumination ring
913 (RIR) setup. Each of the six 525- and 625-nm LEDs are arranged on a ring-shaped board at equal
914 distances. Peltier elements actively cool the LEDs to prevent temperature changes resulting in
915 unstable illumination intensities. 10-nm wide excitation filters are mounted in front of each LED.
916 **C.** Timing diagram to trigger LEDs and camera acquisition: MATLAB controls the DAQ system
917 via digital triggers controlling camera and LED drivers. A different LED illuminates the sample
918 during each frame for near-simultaneous acquisition. The effective frame rate is determined by
919 the length of the four-frame cycle (typically 100 ms). Grey lines next to the camera Fire ALL trigger
920 represent exposure of pixel rows in rolling shutter mode. The Fire ALL trigger is sent when
921 exposure overlaps for all rows. Each LED driver (bottom left) is controlled by the output of a
922 separate AND gate. The Fire ALL trigger is the common input to every AND gate while the
923 individual LED selection triggers are the second input for each AND gate. **D.** Top, light-blue and
924 dark-blue shaded areas represent the 470-nm LED spectrum before and after passing the
925 excitation filter (BP466/40, blue dotted line). Bottom, excitation (solid blue line) and emission (solid

926 green line) spectrum of EGFP-derived $GRAB_{ACh3.0}$ (Jing et al. 2020). **E.** Top, light-orange and
927 dark-orange areas represent the 565-nm LED spectrum before and after passing the excitation
928 filter (BP560/14, orange dotted line). Bottom, excitation (solid yellow line) and emission (solid red
929 line) spectrum of mApple-derived jRGECO1a (Dana et al. 2016). **F.** Top, LED spectra are
930 confined by excitation filters (525 nm in light and dark green; 625 nm in light and dark red before
931 and after passing through the respective excitation filters). Bottom, absorption spectra of
932 oxyhemoglobin (HbO, red line) and deoxyhemoglobin (HbR, blue line) from Prahl (1999). **G.**
933 Spectra of the main dichroic (brown) and detection filter (pink). Light must pass through both filters
934 to reach the camera.

935 **Figure 2: Spontaneous and stimulus-evoked activity in the somatosensory cortex. A.**
936 Average of the first ten images collected during a ten-minute acquisition for each illumination
937 wavelength. The two hemispheres were manually masked around the cranial window. A green
938 polygon was drawn around the right secondary motor cortex, which was determined by
939 registration to the Allen Atlas of the mouse brain. **B.** Spontaneous activity in the right secondary
940 motor cortex (green polygon in panel A) for calcium, acetylcholine (ACh), and oxygenated,
941 deoxygenated, and total hemoglobin (HbO, HbR, HbT). **C.** Ratio maps averaged across 20 trials
942 showing the response to a 2-s, 3-Hz train of air puffs to the right whisker pad. Maps show data
943 from 1.7 s after stimulus onset except for the calcium map, which shows data from 0.1 s after
944 stimulus onset. **D.** Average time course of the stimulus-evoked response in the contralateral barrel
945 cortex (green region in panel C). The pink dashed line indicates when the calcium ratio map in
946 panel C is shown whereas the black dashed line indicates when ACh, HbT and HbO ratio maps
947 in panel C are shown. The grey-shaded area indicates the duration of the stimulus. **E.** Response
948 of the contralateral barrel cortex to individual stimulus trains. The trials are sorted according to
949 the magnitude of the calcium response.

**Figure 3: The aluminum hemisphere shields illumination and reduces pupil constriction during mesoscale imaging. A.** Images of the mouse face 0.5 s before and 5 s after widefield imaging acquisition begins. Green circles highlight the pupils. **B.** Example two-minute pupil diameter time courses showing the off-to-on and on-to-off transition. The grey-shaded area indicates the period when widefield acquisition was performed **C.** Average pupil diameter changes upon beginning of widefield imaging (20 trials; traces show average ± standard deviation). Pupil diameter 1.5-0.5 s before imaging was defined as baseline for each trial. The green-dashed line indicates the start of widefield imaging, the black dashed lines indicate time points of the images shown in panel A. **D.** Comparison of the ratio of pupil size 2-3 s after start of imaging to pupil size 1.5-0.5 s before imaging. Significance was tested with a student's t test.

961 **Figure 1**

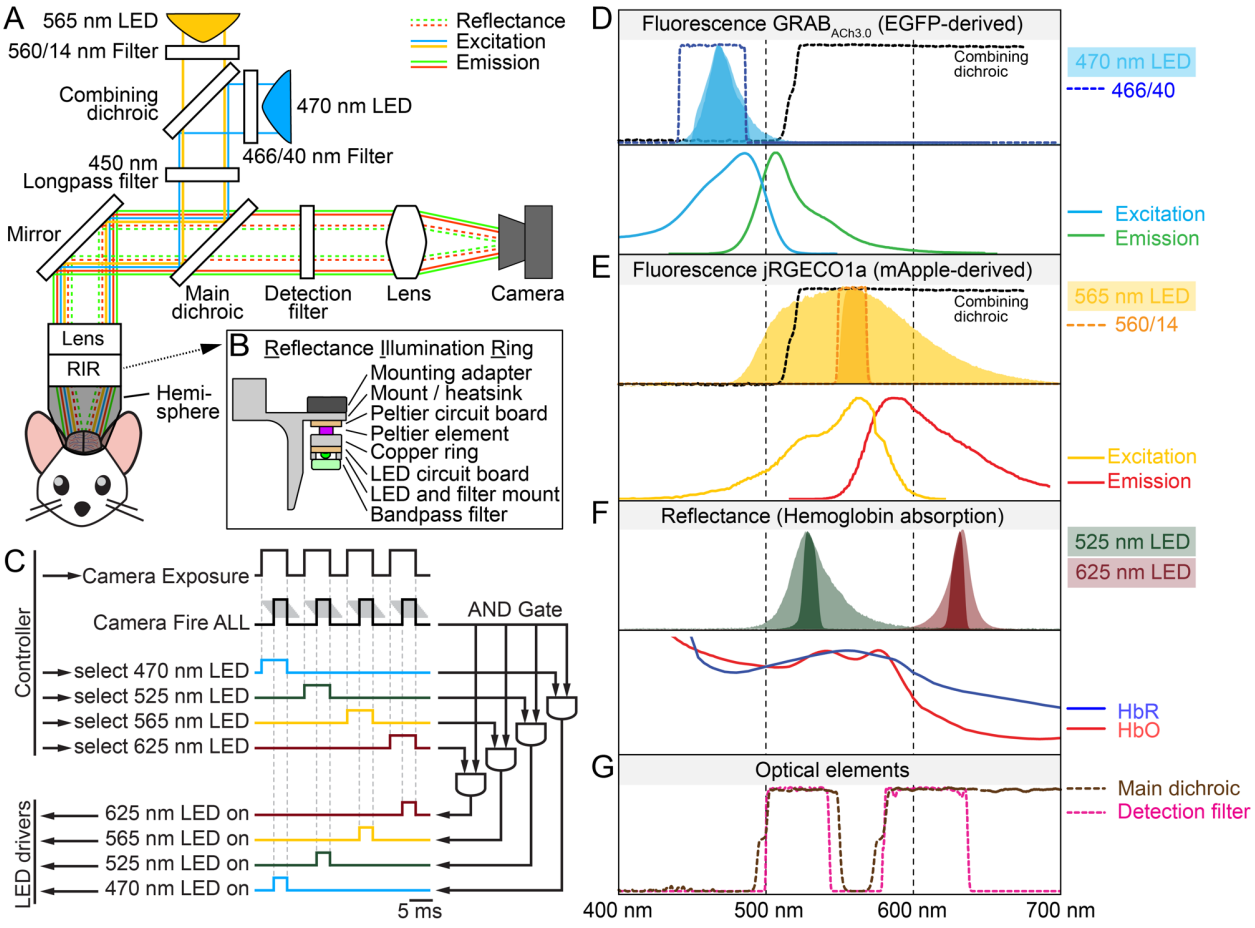


962

963

964 **Figure 2**

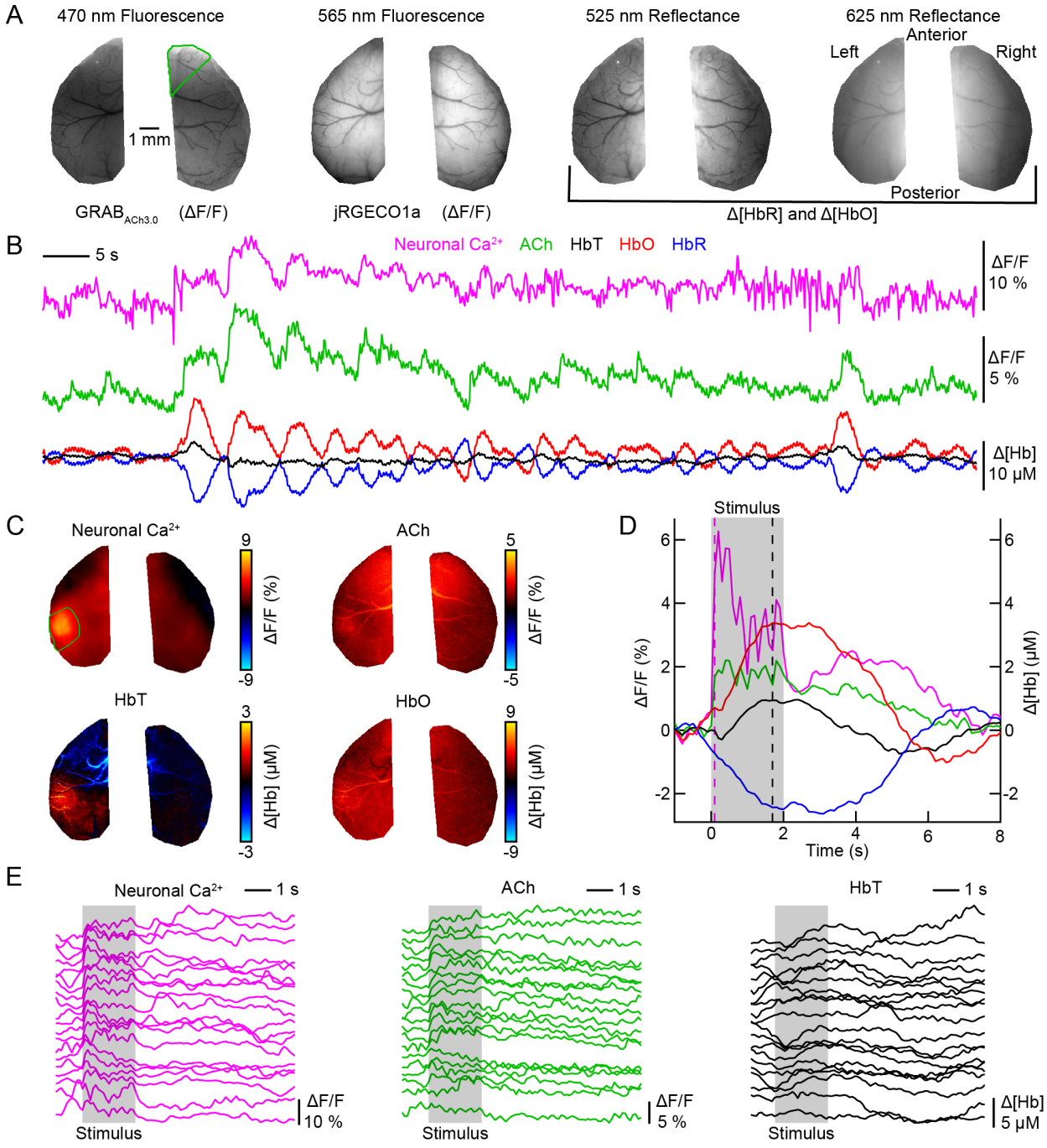


965

966

**Figure 3**

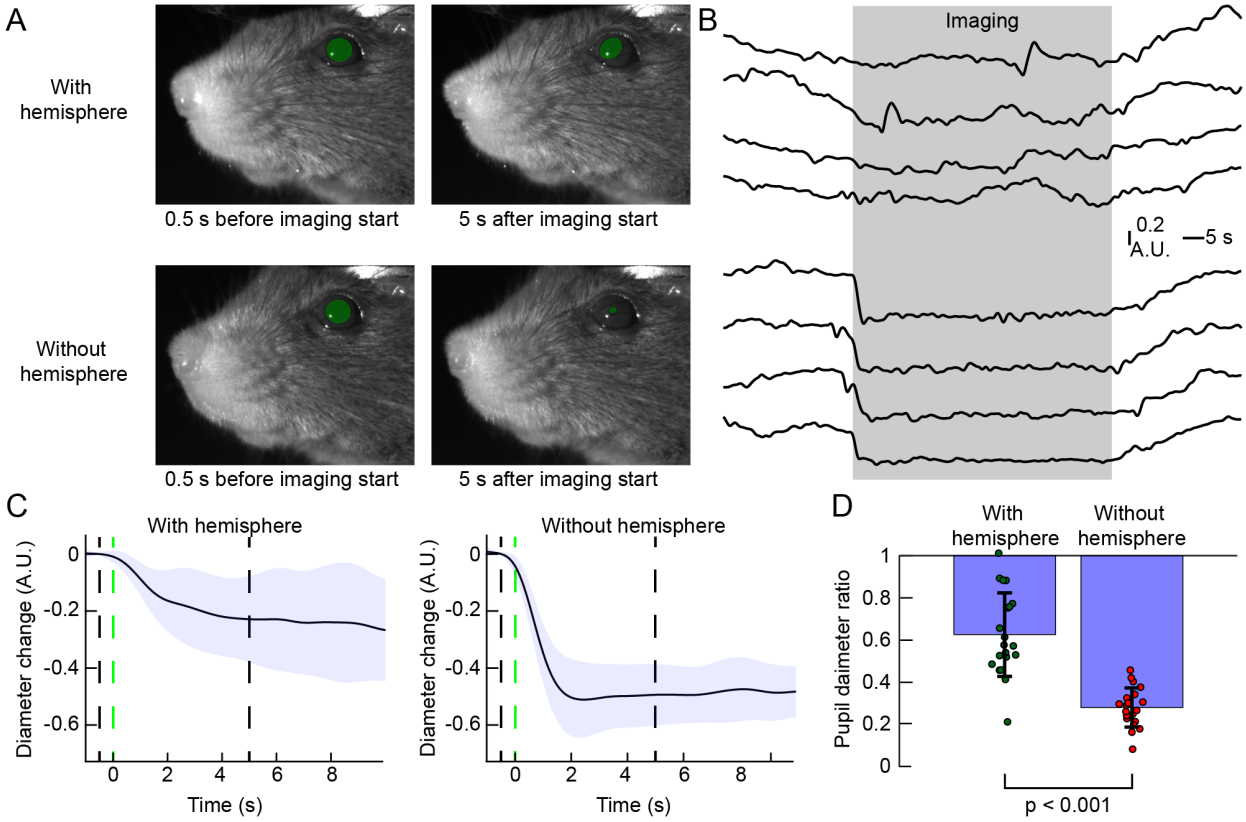
A
With hemisphere
0.5 s before imaging start
5 s after imaging start
Without hemisphere
0.5 s before imaging start
5 s after imaging start
B
Imaging
0.2
A.U.
5 s
C
With hemisphere
Without hemisphere
Diameter change (A.U.)
Time (s)
D
With hemisphere
Without hemisphere
Pupil daimeter ratio
p < 0.001